

Anonymous Referee #1

Received and published: 19 November 2018

GENERAL COMMENTS

This paper describes the creation of maps of height change rates and basal melt rates for Pine Island Glacier's ice shelf, at high spatial resolution and with time-dependence. The authors use a wide range of input data products to produce maps that can resolve the structure of basal melting at scales of individual channel features. This will provide the community with valuable validation for increasingly high-resolution ocean models, and insights into critical processes determining the stability of PIG.

We thank the reviewer for a positive assessment.

Most of the manuscript is a detailed technical description of the processes used to integrate the different data sets and optimize the output products in terms of basal melt rate. I'd hope to see more interpretation of the results in future papers. However, the manuscript is well written, a valuable description of how to get these important products, and even the limited "results" will be of significant interest, so I hope to see the paper published fairly quickly.

Yes, this paper was intended to present the methodological details and shelf-wide melt rates. A follow-on paper describes the spatiotemporal variability with more interpretation.

While there are lots of comments, my major problem in reading the manuscript was in Section 2.9, where I needed more information to really understand the value of the initial-pixel approach to plotting the results.

We added additional clarification in Section 2.9 to emphasize the importance of analyzing local elevation change with initial-pixel approach.

At the same time, this raised the question of whether there was complementary information available in Eulerian dh/dt processing, that might help with the problem that the Lagrangian processing over two years gives a large spatial along-flow average (a few km; larger than the channel and keel cross-flow scale); perhaps Eulerian is better near the grounding line, even with all the extra noise from lateral advection of surface topography?

Yes, there is valuable information in the Eulerian dh/dt products. This is obvious over grounded ice. As the reviewer points out, there is a transition zone near the grounding line, where this information could be complementary to the Lagrangian Dh/Dt products over floating ice. We consider the evolution of 2-year Eulerian dh/dt with the 2-year Lagrangian Dh/Dt melt rates in the follow-on manuscript describing temporal changes in the basal melt rates.

While it is beyond the scope of this paper, a more complex function could potentially be used to merge the Lagrangian Dh/Dt and Eulerian dh/dt values near the grounding zone.

We provide additional comments on this subject under the "Specific Comments" below.

SPECIFIC COMMENTS

Fig. 1: Add labels “Amundsen Sea” and “Pine Island Bay”, and add the grounding line.

We added “Amundsen Sea” label to Figure 1. Did not add “Pine Island Bay” as it would clutter the figure, and did not add grounding line, as this is available for PIG in subsequent figures.

54-55: The laser and radar elevation data sets have very different issues with regard to their value for trend detection, and probably should be described separately.

While this is true, we feel that our existing language is generic enough to be applied to both. Modified slightly to “Elevation data from satellite laser and radar altimetry are further limited by large footprints and sparse repeat-track spacing, with increased uncertainty over areas with non-negligible slopes and/or roughness.”

Fig. 2: Would be useful to plot the most- and least-advanced grounding line on this figure, then explicitly refer to it when discussing GL migration.

Most and least advanced over what time period, and presumably Fig 2D? We feel that plotting multiple grounding lines could make the figure too complicated, and obscure details over the shelf that are important for subsequent discussion. The (Joughin et al., 2016) paper should offer sufficient context for grounding line evolution.

82, Fig. 2c: the color scale for velocity on Fig. 2c saturates at 1 km/yr. But velocity is critical to the interpretation of the spatial scales of basal melt rates, so we need to see the fully resolved velocity field. At a minimum, include it as a full figure in the Supplement, with a color scale that resolves up to 4 km/yr even if it is stretched to improve resolution of speeds <1 km/yr as in Fig. 2c.

The goal with Figure 2C was to show catchment-wide velocities and bring out detail in the south shelf tributary. We elected not to use a logarithmic color ramp, which required saturating the linear color ramp. Figure 1 in (Shean et al., 2017) TC uses a 0-4 km/yr color ramp for the shelf with the same grounding line, and we added a note referring readers to this figure.

92, and Fig. 2: The location of the transverse seabed ridge is sufficiently important in this paper that it should be marked on at least one Main Text figure.

Both reviewers commented on this. We added a label to Figure 2B. This feature is labeled in Figure S1, and we added a note to Figure 2 caption referring the reader to Figure S1 for detailed bathymetry.

140-142: This is *very* technical, and won't make sense to anyone who hasn't worked on this already. The Shean (2016) thesis probably contains this information, but one option is to move this and other very technical stuff in the Supplement where you can give it enough space without bringing the Main Text readers to a complete stop.

We agree that this is technical, but it is one sentence. Additional details are in the ISPRS paper, (not the thesis), which is what is cited, but the specific settings for PIG DEM generation are

different. As this is largely a methods paper, we feel it is important to include this note for improved reproducibility, and we modified language slightly to indicate the settings are intended for advanced ASP users.

196: What is a “DEM-point time offset” ?

This was described in the preceding sentence. We added a new sentence to clarify “We removed points with time offset between the point and DEM timestamp ($t_{altimetry} - t_{DEM}$) of >1 year.” and removed the portion of the sentence that caused confusion.

196-197: The accuracy of control points is small, and won't affect anything reported here. But (a) How is this accuracy determined? and (b) Is it really “accuracy”, or “precision” of a specific measurement over the control?

This estimate is for absolute accuracy of ICESat, ATM and LVIS. We added a note referring the reader to (Shean et al., 2016) ISPRS paper, section 5.1, which discusses this issue.

199-200: I was confused by “with DEM-altimetry time offsets”. Understand now (I think), but it needs more introductory text. I think the problem arises in part because you have these level-4 headers (2.2.1.1 and 2.2.1.2). If you write 2.2.1 as a single sub-section, and just use paragraph breaks to separate WV from SPIRIT discussion, then edit as a single section, it'll be clearer.

Good suggestion, we removed the level-4 headers, and used the newly defined “ $t_{altimetry} - t_{DEM}$ ” instead of “DEM-altimetry time offset”.

202-203, 210: I would like to see some sort of explanation for the 3.1 m bias”. It is laser-to-visible, so there are no snow/firn penetration issues. If it could be traced to, say, different geoids, then it might be a spatially-dependent bias. Or, it is close to just making a sign error on MDT correction.

(Shean et al. 2016) section 6.1.1 includes a discussion of this bias and potential causes. More recent versions of ASP include an atmospheric refraction correction that should mitigate some of this bias. We added “Uncorrected DEMs had an initial mean vertical bias of +3.1 m above the altimetry data (Figure 3), as discussed in section 6.1.1 of Shean et al. (2016), and we applied a -3.1 m vertical correction...”

208-211: This is another complex “explanation” that requires more familiarity with the topic than many readers will have.

This is a note on additional processing required for one problematic SPIRIT DEM, and we feel it is important to document for reproducibility.

224: While it won't change your results, Andersen and Knudsen (2009) is a very old citation for MDT: if you are really using that old a product, you might want to change for more recent versions.

We agree that this will not change the results. We welcome the reviewer to suggest an updated reference to use here.

295-300: I think I follow what you are doing, but (a) you don't explain WHY the reverse- ordering is a good approach, and (b) it suggests to me that the optimum time stamp for the resulting product may not be as centered on the central image time as I would have expected.

The paragraph above this section and introductory sentence provide justification for why this ordering is necessary. We also tested ordering with earliest timestamps on top, and timestamps closest to an arbitrary date (e.g., Jan 1) on top. In the end, the reverse ordering scheme provided best continuity for the available DEMs. Separate timestamp layers provide the corresponding DEM timestamp at each pixel in the ordered mosaics, for later analysis. As described in the text, we also generated weighted average composites for all available DEMs each season. None of this is relevant for the basal melt rate calculations, which use individual DEMs, not these mosaics.

346 ff: Everything before this point is describing the input data sets. Starting here, you are describing what you get in terms of products you really want to get at. Overall, the current Section 2 is too piecemeal, as evidenced by getting into level-4 subheaders.

Perhaps there is a better organization where Section 2 is just about the input data, then Section 3 (made up of 2.8-2.10) could be "Deriving elevation changes and basal melt rates". That way you'd never get to level-4 subheaders, and the transition from "data setup" to exploitation would be clearer.

This is a great suggestion, and helps with organization. We separated into Section 2 and Section 3 as suggested.

362 through eq. (9): (a) "then compute ice-equivalent freeboard thickness: $H = \dots$ ". This slowed me down for a while. H is "ice thickness assuming no firn air", right? Maybe this would be clearer if eq. (8) was expressed " $h = \dots$ " or it might just need better lead-in words before eq. (8). (b) I also had to think a bit about eq. (9). You apply divergence to firn air (d). However, you don't allow for any time rate of change of local firn air content. I think you end up accounting for this later, but here you describe it as "dropping the CONSTANT d from ..." which seems unjustified at this time.

To avoid confusion removed "(after removing firn-air content d)" from the sentence above eq 4, so that this reads "ice-equivalent thickness H can be expressed as... ". We also modified eq 8 to use H_f instead of H .

Yes, we are assuming time-invariant (constant) firn air content. We modified the text above Equation 9 to clarify: "This ice-equivalent freeboard thickness H_f can then be substituted for H into in Equation 7. We assume that any changes in d , ρ_w and ρ_i are negligible during our study period, and the DH_f/Dt term reduces to Lagrangian surface elevation change (Dh/Dt), resulting in a modified mass-conservation expression for a column of floating ice."

373 ff: If you decide that section 2.8 should stay in the existing section 2 (see comment two above here), then consider maybe Sections 2.9 and 2.10 into a separate section ("3. Basal melt rate estimation"?). Whatever you do, restructure to avoid level-4 sub- headers.

We restructured as suggested in previous comment

405-410: This para needs to be revised. Start by explaining the concept of channels and keels. At the moment, you introduce the idea of “vertically variable” melt rate before I have any idea in what way a melt rate might vary “vertically” at a single site.

We modified this paragraph, but do not feel it is necessary to explain the basic concept of channels and keels, as these are introduced earlier in the text. The existing description as “features with variable draft” should be sufficient. Changed to “End member #1 assumes a fixed 3D “melt rate field” within the ocean cavity beneath the PIG ice shelf that varies spatially but not temporally, so that features with variable draft (i.e., keels and channels) melt at different rates as they advect through this field.”

444-450, and more generally 419-451: I found this text very difficult to follow the first few times I read it, and maybe it is still a problem.

We acknowledge that this is a complex concept. This section underwent several revisions before submission to improve readability, and we feel it is sufficient. If the reviewer has specific comments on how to improve, we are open to make additional changes.

Given that Lagrangian-derived melt rate is only calculated on 1-2 year time periods, how can you really get information at smaller scales than is associated with advection over this time? The initial-pixel product is more detailed (Fig. 8), but you don’t really know anything about whether it varies on such small scales.

We disagree with this conclusion. This is precisely why we outlined the two end members for melt rate field and explored two different approaches for melt rate calculation.

The “along-flow” approach can be thought of as a form of tomography - multiple features with different start and end points pass through the same location on an Eulerian grid can provide enhanced detail on the melt rate field (end member #1) at that location. The “initial-pixel” approach is calculated at the inherent resolution of the DEMs, and if melt rates are dictated by local geometry (end member #2), then we are resolving melt rates at these scales.

The description of the differences and limitations of the two methods is honest, so it’s okay as-is, but it raises the question of whether there is valuable complementary information in an EULERIAN dh/dt calculation, especially with regard to the region near the grounding line where melt rates change rapidly. Maybe the extra noise in the Eulerian calculation is worth it in this case?

This is a good question. One can consult Figure 8 (long-term Eulerian dh/dt , now with grounding line plotted for context) for some insight. After the ice plain ungrounding events that ended in ~2008, there is limited elevation change (even slightly positive) immediately downstream of the new grounding line. However, we continue to see significant thinning in the Lagrangian Dh/Dt products due to basal melting and divergence. Compare Figure 8D with Figure 9 (updated numbering scheme).

As mentioned in general comments, we consider this question further in the follow-on manuscript.

486: The velocity error derived from look angle and elevation uncertainty makes sense. However, you cited tide and IBE error as 0.1 m. Why do you need to use the full tide, rather than the error, in this calculation?

The velocity maps were generated using the established methodology of Joughin (2002), which does not correct for tidal variations over floating ice shelves, so the 0.5 m accounts for expected tidal magnitude. As described in section 2.2.2, we corrected surface elevation data over floating portions of the PIG ice shelf for tide and the inverse barometer effect. The quality of these corrections was evaluated in (Shean et al. 2017), which is cited in the text.

Figure 7: (a) Add grounding line(s) to these plots. (b) Maybe make the ICESat and ATM tracks a bit wider so it's easier to see the color shading of the tracks. (c) {In caption}: There's no such thing as "ICESat-1" is there? Just "ICESat". (d) A "North" arrow would be useful (on one panel).

We added the grounding line, which improves interpretation.

The tracks are part of the gridded dataset, so their width is based on the grid cell size. We prefer to keep them sparse, which is closer to the actual ICESat footprint.

Good catch - yes, it's ICESat, not ICESat-1 - fixed all instances.

Figure 8: I found the arrows harder to find than they should be. Perhaps use a white outline around the edge of the arrow, and/or add a shaft to the arrowhead, and/or use lighter shades of each color as the background is generally dark.

Added white outline to arrows in Figure 8.

537-540: Even with the colorbar stretch in the lower panels of Fig. S4, it is hard to see detail of melt rate on the North ice shelf, and even much of the South. Maybe choose an even smaller range for the lower panels of Fig. S4, or even add a third set of panels at a lower range, designed specifically to highlight North and South ice shelves.

We feel the perceptually uniform color ramp in Fig S4 provides sufficient contrast to distinguish meaningful melt rate variations on the North and South shelves. Melt rate differences of <5 m/yr are within uncertainty.

609-610: How can Payne et al. (2007) be evidence both for "significantly higher than past estimates" but also "more consistent with the Payne et al. (2007) estimates" ?

Good catch. Removed citation from first sentence.

611-613: You can't really claim that your estimates are less than past estimates, when they "fall within reported uncertainty". It would be better to acknowledge first that they are the same within uncertainty, but then speculate on "maybe they really are smaller, which we'd explain as ..."

This is true. We modified the text to clarify.

625-628: The other advantage to Ross and FRIS is that they are further south where ICESat orbits are closer together.

Good point. Added a note on this.

TECHNICAL CORRECTIONS

Given the oceanographic interest, the use of “shelf” instead of “ice shelf” can be confusing. I’d recommend always saying “ice shelf”.

This is a good suggestion. We attempted to correct all ambiguous instances of “shelf” to “ice shelf”

When referring to a paper, I tend to go with “BY Smith et al.” rather than “IN Smith et al.” unless it refers to a specific items like a figure or an equation. Just a more direct credit to the authors.

This is also a good suggestion. Modified where appropriate.

The use of the dash between dates is variable and confusing. “from 2008-2015” might mean “from 2008 to 2015” or “during the period 2008-2015”. Try to read it out, and see if just using “to” or “between XXXX and XXXX” would work better.

We attempted to modify instances where this might be confusing. We attempted to consistently use em-dash for date ranges. Defer to TC editorial staff on best practices.

Present/past tense: Wanders a bit, e.g., line 168, probably should have “mask” => “masked” and “remove” => “removed”. Also in Section 2.1.3, and several other places.

Fixed these instances, and attempted to improve consistency throughout paper.

Try to avoid “Figure/Table X shows that”. Usually it’s possible to give the science, then the figure cite parenthetically.

We appreciate the suggestion, but this is an author-specific style decision.

556, 603, 630: Remove all “We note that”; not needed.

Good point. Removed all instances

“ICESat-1”: My understanding is that, even though there is now an ICESat-2, the original laser mapping mission is still called “ICESat”, not “ICESat-1”.

Fixed as described in previous response.

10: “directly and indirectly” presumably refers to direct loss from the ice SHELF, and indirect loss from the ice SHEET, but it immediately slows down the reader.

Yes, this refers to the loss from sub-ice-shelf melting and the dynamic response leading to increased discharge. But removed to avoid confusion

38-48: Break this sentence up; use separate sentences for each major methodology.

We disagree that separate sentences are needed for each methodology and prefer the concise presentation (albeit with many references).

74-75: I expected to see a cite to Shepherd et al. 2018 (IMBIE) here.

Added

82: “Two additional ice shelves”. Not really. North and South ice shelves are part of PIG, and you count them as part of PIG.

Good point. We modified to read:

“Shear margins with width ~2-4 km separate the main shelf from the northeast (“North shelf”) and southwest (“South shelf”) sectors of the PIG ice shelf (Figure 2D)”

83-86: Confusing construction, and I’m not sure it’s even true. It is true that velocities of the N and S ice shelves are relatively small, but the quoted thickness ranges are similar to most of the main trunk. In fact, the S shelf is thicker, on average, than most of the Main trunk. (Fig. 2d treated as a thickness proxy).

This is a valid point. We were comparing to the thickness closer to the main shelf grounding line. We removed discussion of thickness for N and S shelves, and only discuss velocity.

Changed to:

“In general, surface velocity is relatively slow (<100–500 m/yr) over the North and South shelves, except for a fast-flowing tributary of the South ice shelf with velocity of ~1 km/yr and thickness of ~1 km near the grounding line (Figure 2)”

87, Fig. 2A: Please add the catchment boundaries to this figure.

We do not feel this is necessary, as the topography in 2A shows the catchment, and it is not relevant for the main focus of the paper.

91-92: Probably don’t need a paragraph break here.

Removed

109-110: Sentence starting “Water at ...” needs a cite or two.

Added (De Rydt et al., 2014; Dutrieux et al., 2014b) citations to the text.

135-136: Fig. 1 shows the “ASE” coastline, not the “West Antarctic” coastline.

This is a fair point. But it also spans the Bellinghousen Sea, and perhaps a portion of the Ross Sea, depending on where partitions are drawn.

Changed to “for the Amundsen and Bellinghousen Sea coastline of West Antarctica”

186: maybe “extend the ... record BACK to 2003”. When I first read it, sounded like 2003 was later than most data.

Changed

201: revise to “There is a ... (Fig. 3, Table 2).”

Changed to:

“The ICP co-registration provided translation corrections for 368 of 575 DEMs over the PIG catchment, with a significant improvement in multiple quality metrics following co-registration (Figure 3, Table 2).”

242-243: Isn't there also a Ben Smith (co-author) explanation of this approach for processing of ICESat along-track data?

We are not entirely clear about the reviewer's suggestion here - is there a citation we should consider including? D. Shean implemented the methodology described in the text after discussion with B. Smith.

248: "the main shelf and fast-flowing trunk". Aren't these the same thing? Okay, no, I guess the "trunk" is the grounded ice, so say "main {ice} shelf and fast-flowing GROUNDED trunk"

Changed to "main ice shelf and fast-flowing grounded ice stream"

263-264: probably just use "high-priority areas such as ..." and delete the "i.e., and out parentheses.

Changed as suggested

312: "m/px" is a strange abbreviation. Maybe cleaner to use "m/pixel"

This is a common abbreviation in the remote sensing literature. Changed to "...500-m ALOS and LS8 products..."

314: "over a ~11-189 day period" reads awkwardly.

Deleted this sentence, as details are in citations.

317: I have no idea what "barycentric interpolation" is.

<https://codeplea.com/triangular-interpolation>

336: {FYI} Mueller et al. (2012; JGR) used bed interpolation along flow lines to make a sub-ice-shelf bathymetry grid for Larsen C.

We were not aware of this paper, thank you for the reference. We added a citation, though the interpolation methodology used here is continuous for the bed and bathymetry, with many more observational constraints and more sophisticated regularization.

379: "Lagrangian Dh/dt basal melt rates" doesn't make sense. Maybe "basal melt rates based on Lagrangian height-change measurements"

Modified to "basal melt rates from Lagrangian Dh/Dt observations"

399: "from A single, fixed"

Changed to "fixed"

400: "step but, in practice, ..." (move first comma).

Removed "in practice"

401: "useD", "substituted"

Fixed

521: "downstream of THE grounding line"

Fixed

555: "over keels" is ambiguous; "on keels" or something else would be clearer.

Changed to "on keels"

577: Why quotation marks around "resolution" ?

Removed quotation marks

Anonymous Referee #2

Received and published: 25 March 2019

This paper presents an extensive study of high-resolution satellite DEMs for determining elevation changes and ice-shelf basal melting of Pine Island Glacier in unprecedented detail. The amount of data and complexity of the analysis are impressive and well justified. A lot of care has been taken to find optimum methodologies and complementary ways of representing basal melt rates in a spatial domain that is constantly evolving. The high technical quality of the paper will make it a benchmark for related studies in the future, and the detailed results of basal melting will be highly useful for modellers.

The glaciological part of the paper is somewhat drowning in all the technicalities, but has a high potential for follow-up papers concerning links with ice-ocean interactions. It is therefore still well suited for a journal like the Cryosphere.

We thank the reviewer for this favorable assessment. Indeed, a follow-on publication highlights interesting results on the temporal evolution of melt. We hope that the current paper will satisfy both technical readers and those who are more interested in the main results can skip the detailed methodology.

The main things I would like to see improved before publication are the overly fragmented sections and the figures which are sometimes too excessive and not as informative as they could have been. More details on that are provided below, first on the figures and then on the manuscript text in line-by-line comments and edits which are mostly of minor nature.

We reorganized and combined sections in the text and modified several figures, as described in the specific comments.

Figure comments and suggestions:

Fig. 1: Although an impressive data set, I do not see the purpose of these regional DEM figures when the paper is all about PIG. Figure 2d would be a better opening figure, potentially with Fig. 1A or similar as an inset to show the location of PIG within West Antarctica. The present Fig. 1 could still be included in the Supplement, and in that case grounded ice and ocean areas could be masked out in panel b to highlight the ice shelves.

We appreciate the reviewer's point, but Figure 1 provides context for Figure 2 and the PIG DEM time series. We also feel it is important to document the entire DEM dataset that was generated, to highlight potential for other ice shelves in the region.

Fig. 2: The upper three panels could be split into a separate figure to better highlight the detailed and nice ice shelf one. The ice shelf outline is hardly visible in panels b and c, which should be improved for context, preferentially with bedrock and velocity close-ups of the ice shelves like the upper third panel of Fig. S1. That would be a good opportunity to highlight the

“transverse seabed ridge” in the main paper, as well as velocity variations on the main ice shelf which are totally saturated in Fig. 2c. In that case, a new multi-panel figure would definitely be needed and could replace the current Fig. 1.

As suggested, we split Fig 2A-C and Fig 2D. The latter is now Figure 3 (with subsequent figure numbers updated). We added a label for “TSR” to show location of transverse seabed ridge on a figure in main text.

Fig. 2 caption: I assume that it is over Bedmap2 surface hillshade, not “Bedmap2 DEM”.

This is the WorldView/GeoEye DEM composite embedded in the Bedmap2 DEM, with a shaded relief map derived from the combined product.

For panel B; “...anisotropic interpolation of available data” (or be more specific).

Changed to “Bed topography from anisotropic interpolation of radar-derived ice thickness (Section 2.6)”

Unless grids or coordinates are included in any of the figures, the caption should say something about the location and map projection.

Added “Projection is Antarctic polar stereographic (EPSG:3031).” to Figure 1 caption.

Fig. 3: Could be moved to the supplement, but since this paper focuses so much on methodology it is okay to keep here. Please define in the caption what the dashed lines (mean or median of all errors?) and error bars represent (16-84% spread?). The small text at the top is somewhat cryptic and should be removed or included in the caption.

We modified the caption as suggested. As stated in the caption, additional details on interpreting this figure can be found in [\(Shean et al. 2016\)](#).

Fig. 4: This is a powerful illustration of the importance of careful co-registration for studies like this. To be improved: Make panel numbers as in preceding figures. Define what “Count” is. Include the PIG grounding line in white since that partly coincides with where the DEM variability is higher.

We added panel letter labels and the grounding line, and modified the caption to better define count as per-pixel DEM count.

Fig. 5: Panel numbers missing.

We do not feel panel labels are needed for this figure, as years are listed. Defer to TC editorial staff.

Fig. 6: This figure and the elaborate caption give a good explanation for a very complex methodology, but repeats and overlaps with the manuscript text which is unnecessarily fragmented into a series of sub-sections. These parts need to be better harmonized, potentially by moving much of the caption into the main text and removing repeated information from there.

We acknowledge that this caption is long. But also acknowledge that many readers may not read detailed methodology in text. We prefer to keep the extended caption and detailed description in the text. As stated earlier, we reorganized these sections to alleviate fragmentation.

Fig. 7: A shaded relief would be a nicer background than black in panels a and c. Ice shelf outlines (in white) would also be helpful in all panels to see relations with dh/dt patterns.

We added the grounding line, as suggested by both reviewers. We experimented with a shaded relief background, but felt that it obscured many of the ICESat tracks with near-zero elevation change (white), so we kept solid black background to make sure that these tracks are visible.

Fig. 8: Switch order of panels similar to the order of discussion in the text? I am not sure if the color scale is optimum, a lot of the ice shelf appear dark with no visual contrast.

Good suggestion to switch panels for order of appearance. We experimented with several color stretches, and this one (with contours) was chosen to bring out as much detail as possible over the main shelf. The reviewer seems to be focused on small melt rates over the North and South shelves, which are small, within measurement uncertainty, and not the focus of this work.

Fig. 9: It is a very good idea to separate channels and keels in the figure, but in the end it is actually difficult to see clear differences between panels and that also makes some of the main conclusions of the paper weaker. Have you tried other color bars or different scaling to see if differences may come out more clearly? Panel numbers are also missing.

We disagree that it is difficult to see differences. And yes, we experimented with several different color stretches and settled on these to best capture the range of melt rates for channels/keels on both the inner and outer shelf.

Fig. S1: Include panel numbers. The header “anisotropic interpolation” is confusing unless more details are provided (interpolation of what?).

This is described in Section 2.6 of the main text, with a citation.

Fig. S2: Something wrong with the reference here. I assume you want to refer to the similar Fig. 3 in the main manuscript. See also my comment to that figure.

Yes, it should reference Figure 3 in the main text. It looks like this was a cross-reference that was not updated. Fixed.

Fig. S4: See comment to Fig. 8. Although different colorbar stretches here are helpful C3 for interpretation of Fig. 8, I still feel that a lot of area appear dark without visible contrast.

Addressed with earlier comment. It is impossible to choose a “perfect stretch” for this dataset. The stretches for the figures were carefully chosen to emphasize main points. We hope that any readers who are unsatisfied with the color ramp will download the data and visualize with their preferred stretch.

Line-by-line comments and edits:

62-66: All the information and parentheses make this sentence hard to read. Split/rewrite or remove some content. This is also good to keep in mind elsewhere in the manuscript during revisions.

We are following standard citation formatting for TC. We feel that it is important to include these citations, and feel that this is the most concise way to do so. If these were numbered superscript citations, as in a Science/Nature paper, this would be less of an issue.

67: To be clear; "... across the grounding line of the South ice shelf"

Fixed

82: Fig. 2C is not a good reference here since it saturates at 1 km/yr. Remove.

Removed

83: The "South shelf" has already been introduced at L67, but more clearly here. Perhaps the order of the text should be switched or L67 can be simplified/removed.

Yes, this is true, but we would rather provide historical context for PIG before getting into detailed geography for the study period. Changed to:

"...with a corresponding increase from ~10 to ~12 Gt/yr across the grounding line of the South PIG ice shelf (e.g., the "Wedge" catchment of Medley et al. (2014))"

92: This is an important feature and therefore it is somewhat unfortunate that the reader is only referred to the supplement. However, it is also visible in Fig. 2B if the ice shelf outline is made thicker to highlight the relevant area, i.e. reference (Fig. 2B and S1).

Changed to "Figure 2B and S1". We split figure 2 and added label for 2B.

198: Four levels of sections is quite elaborate for a single research paper. I think that subdivision into 2.2.2.1 and 2.2.1.2 is more confusing than helpful.

Reorganized to remove all level-4 headings

228: I assume that this applies to the ice-shelf side of the grounding line. Suggestion for rewrite: "To provide a smooth transition from fully grounded ice to freely floating ice, we defined the coefficient ... downstream of the grounding line:"

Good suggestion, changed as suggested.

Eq. 3: t is not defined

Modified to reiterate that t represents time

257-259: It is not clear what the "tilt tolerance" is and how it was used.

We changed "tilt tolerance" to "limits for tilt magnitude" - this is another set of weights in the least-squares optimization.

267: Define or remove CE90/LE90

These are 90th percentile of circular/linear error - common accuracy metrics in remote sensing literature. Removed for clarity, as the reader can reference the Shean et al (2016) paper, where these terms are defined and discussed.

335: Mention “anisotropic” here to make the link with Fig. S1 obvious.

Good suggestion. Added.

345: How was the finer interpolation of the coarse RACMO data done?

Changed to “We generated gridded RACMO SMB products with the same extent and spatial sampling as the DEM and velocity products using bicubic interpolation.”

352: How was firn air content removed? As a constant or time-variable?

This is discussed in Section titled “Uncertainty and sources of error”. We added a sentence on this to address comment by Reviewer #1.

353: Here you talk about surface accumulation, earlier SMB. Be consistent.

Good catch. Changed to SMB

365: What do you mean by “dropping the constant d”? It is probably reasonable to treat it as a constant, but that should be briefly discussed/justified, e.g. in section 2.7.

This was addressed in response to Reviewer #1.

418: I think the word “product” is misleading here since it’s more a description of how the calculation is done, whereas composites/mosaics are described later.

Removed “products”

443: Is a separate section needed? It is all almost about the initial-pixel approach, and the last sentence can be moved to line 417.

We prefer a separate section that compares the two approaches and ties back to the end member scenarios described earlier.

We moved the last sentence to line 417, but in the end, felt that it was redundant and removed entirely

482: The simplified assumption of a constant firn air content in space and time is probably a minor issue for PIG, but not for most other ice shelves in Antarctica. A brief discussion or recapture of the cited reference would therefore be appropriate.

Yes, and our +/- 2 m uncertainty should account for this spatial and temporal variability. As this paper focuses on PIG, we do not feel it is necessary to comment on this issue for other ice shelves. We look forward to future higher-resolution SMB and firn air content products that can further constrain this important correction for PIG and other shelves with lower basal melt rates.

559: In this section you discuss characteristics of channel and keel melting shown in Fig. 9, but refer to arrows in Fig. 8. That is confusing, and even more so when some features like the “prominent longitudinal keel” is generally visible in Fig. 8, but not in Fig. 9 where keels and channels are separated.

We believe that the arrows in Figure 8 are sufficient. Figure 9 is a composite of all years, not a snapshot view of the shelf. During the 2008 to 2015 period, the shelf experienced a rotation, as

documented by (Christianson et al., 2016; Jeong et al., 2016). As a result, the longitudinal channels/keels shifted their position on the Eulerian grid. When creating a weighted average composite of keels from all years, this feature is not as prominent due to this motion.

593: It is very hard to actually see this in Fig. 9. Is it possible to find a better color scheme that makes this key point more convincing?

We modified the color scale for Figure 9.

656: FDM is not used in the manuscript as far as I can see (constant firn air content)

Good catch. This was used in the (Shean et al. 2017) TC paper, but we removed any mention of FDM in this paper.

Table 3: Define “n”

Changed to “Minimum number of DEMs”

References:

Christianson, K., Bushuk, M., Dutrieux, P., Parizek, B. R., Joughin, I. R., Alley, R. B., Shean, D. E., Abrahamsen, E. P., Anandakrishnan, S., Heywood, K. J., Kim, T.-W., Lee, S. H., Nicholls, K., Stanton, T., Truffer, M., Webber, B. G. M., Jenkins, A., Jacobs, S., Bindschadler, R. and Holland, D. M.: Sensitivity of Pine Island Glacier to observed ocean forcing: PIG response to ocean forcing, *Geophys. Res. Lett.*, 43(20), 10,817–10,825, doi:10.1002/2016GL070500, 2016.

Jeong, S., Howat, I. M. and Bassis, J. N.: Accelerated ice shelf rifting and retreat at Pine Island Glacier, West Antarctica, *Geophysical Research Letters*, 43(22), 11,720–11,725, doi:10.1002/2016gl071360, 2016.

Joughin, I., Shean, D. E., Smith, B. E. and Dutrieux, P.: Grounding line variability and subglacial lake drainage on Pine Island Glacier, Antarctica, *Geophysical Research Letters*, 43(17), 9093–9102, doi:10.1002/2016gl070259, 2016.

Shean, D. E., Alexandrov, O., Moratto, Z. M., Smith, B. E., Joughin, I. R., Porter, C. and Morin, P.: An automated, open-source pipeline for mass production of digital elevation models (DEMs) from very-high-resolution commercial stereo satellite imagery, *ISPRS Journal of Photogrammetry and Remote Sensing*, 116, 101–117, doi:10.1016/j.isprsjprs.2016.03.012, 2016.

Shean, D. E., Christianson, K., Larson, K. M., Ligtenberg, S. R. M., Joughin, I. R., Smith, B. E., Max Stevens, C., Bushuk, M. and Holland, D. M.: GPS-derived estimates of surface mass balance and ocean-induced basal melt for Pine Island Glacier ice shelf, Antarctica, *The Cryosphere*, 11(6), 2655–2674, doi:10.5194/tc-11-2655-2017, 2017.

Ice shelf basal melt rates from a high-resolution DEM record for Pine Island Glacier, Antarctica

David E. Shean¹, Ian R. Joughin², Pierre Dutrieux³, Benjamin E. Smith², Etienne Berthier⁴

¹Department of Civil and Environmental Engineering, University of Washington, Seattle, 98185, USA

²Applied Physics Laboratory, University of Washington, Seattle, 98105, USA

³Lamont-Doherty Earth Observatory, Columbia University, Palisades, 10964, USA

⁴LEGOS, CNES, CNRS, IRD, UPS, Université de Toulouse, Toulouse, France

Correspondence to: David E. Shean (dshean@uw.edu)

Abstract. Ocean-induced basal melting is responsible for much of the Amundsen Sea Embayment ice loss in recent decades, but the total magnitude and spatiotemporal evolution of this melt is poorly constrained. To address this problem, we generated a record of high-resolution Digital Elevation Models (DEMs) for Pine Island Glacier (PIG) using commercial sub-meter satellite stereo imagery and integrated additional 2002–2015 DEM/altimetry data. We implemented a Lagrangian elevation change (Dh/Dt) framework to estimate ice shelf basal melt rates at 32–256-m resolution. We describe this methodology and consider basal melt rates and elevation change over the [PIG ice shelf](#) and lower catchment from 2008 to 2015. We document the evolution of Eulerian elevation change (dh/dt) and upstream propagation of thinning signals following the end of rapid grounding line retreat around 2010. Mean full-shelf basal melt rates for the 2008–2015 period were ~82–93 Gt/yr, with ~200–250 m/yr basal melt rates within large channels near the grounding line, ~10–30 m/yr over the main shelf, and ~0–10 m/yr over the North and South shelves, with the notable exception of a small area with rates of ~50–100 m/yr near the grounding line of a fast-flowing tributary on the South shelf. The observed basal melt rates show excellent agreement with, and provide context for, *in situ* basal melt rate observations. We also document the relative melt rates for km-scale basal channels and keels at different locations on the [ice shelf](#) and consider implications for ocean circulation and heat content. These methods and results offer new indirect observations of ice-ocean interaction and constraints on the processes driving sub-shelf melting beneath vulnerable ice shelves in West Antarctica.

25 1 Introduction

The Amundsen Sea Embayment (ASE) of the West Antarctic ice sheet (WAIS, [Figure 1](#)) has experienced significant acceleration, thinning, and grounding line retreat since at least the 1970s ([Joughin et al., 2003](#); [Konrad et al., 2018](#); [Mouginot et al., 2014](#); [Rignot et al., 2014](#); [Rignot, 1998](#)). During this period, regional mass loss increased to present-day estimates of ~100–120 Gt/yr ([Medley et al., 2014](#); [Sutterley et al., 2014](#); [Velicogna et al., 2014](#)). These changes appear to be linked to changes in the meridional transport of dense, relatively warm (~0.5–1.2°C, up to +2–4°C above *in situ* freezing point) ([Jacobs](#)

Deleted: 3

Deleted: directly and indirectly

Deleted: PIG shelf

Deleted: -

Deleted: Figure 1

Field Code Changed

Deleted: (Joughin et al., 2003; Konrad et al., 2018; Mouginot et al., 2014; Rignot et al., 2014; Rignot, 1998)

et al., 2012, 2011; Rignot and Jacobs, 2002)) Southern Ocean sourced Circumpolar Deep Water (CDW) onto the continental shelf (Dutrieux et al., 2014b; Jacobs et al., 1996; Pritchard et al., 2012; Shepherd et al., 2004), where it is funnelled along deep
40 troughs toward the vulnerable grounding lines of large ice streams with reverse bed slopes (Jenkins et al., 2010). Marine ice sheet grounding lines on reverse bed slopes are inherently unstable (Schoof, 2007; Weertman, 1974), and this focused melting can trigger further grounding-line retreat, acceleration, and dynamic thinning (Joughin and Alley, 2011). Approximately 75% of the West Antarctic Ice Sheet is grounded below sea level, raising concerns about large-scale collapse due to this instability, which could lead to ~3.3 m of global sea level rise (Bamber et al., 2009).

45 Over the past ~30 years, numerous observational studies have estimated Antarctic ice shelf basal melt rates (e.g., Table S2 of Rignot et al. (2013)). The scope of these efforts ranges from continent-wide remote-sensing inventories (Depoorter et al., 2013; Paolo et al., 2015; Pritchard et al., 2012; Rignot et al., 2013; Shepherd et al., 2010) to detailed analysis of individual shelves (Berger et al., 2017; Dutrieux et al., 2013; Joughin and Padman, 2003; Moholdt et al., 2014; Wilson et al., 2017). Various methods were used for these assessments, including mass budget ("input-output" or "flux gate") methods (Depoorter et al.,
50 2013; Rignot et al., 2013), satellite laser altimetry (Pritchard et al., 2012), satellite radar altimetry (Paolo et al., 2015; Shepherd et al., 2004), field observations with phase-sensitive radar (Dutrieux et al., 2014a; Jenkins et al., 2006; Langley et al., 2014; Marsh et al., 2015; Stanton et al., 2013), *in situ* oceanographic observations from autonomous submersibles (Dutrieux et al., 2014b; Jenkins et al., 2010), borehole-deployed instrumentation (Kobs et al., 2014; Stanton et al., 2013), traditional mooring or ship-based oceanographic observations beyond the ice shelf margins (Jacobs et al., 1996, 2011; Jenkins et al., 1997, 2018),
55 and ocean circulation modeling (e.g., Dutrieux et al., 2014b; Payne et al., 2007; Schodlok et al., 2012).

Each of these methods has advantages and disadvantages, differing spatial coverage/resolution, temporal coverage/resolution, measurement uncertainty, and logistical cost. Many methods require multiple input datasets, and the available data often span different time periods. For example, most previous mass budget analyses combine elevation change rates derived from ICESat
60 altimetry between 2003 and 2008 – a time period characterized by significant change and imbalance in the Amundsen Sea Embayment region – with velocities from a fixed year or a composite mosaic from multiple years (e.g., mosaic of Rignot et al. (2011)). Elevation data from satellite laser and radar altimetry are further limited by large footprints and sparse repeat-track spacing, with increased uncertainty over areas with non-negligible slopes and/or roughness.

Here, we describe the methods to process and analyze a new dataset of high-resolution DEMs from stereo satellite imagery for Pine Island Glacier (PIG), Antarctica. We use these products to characterize the spatial distribution of ice shelf basal melt and
65 elevation change over the past decade, and evaluate relative melt rates for km-scale ice shelf thickness variations. These methods and results provide a foundation for forthcoming detailed analyses of spatiotemporal evolution of PIG ice shelf basal melt rates and comparisons with ocean observations.

1.1 Pine Island Glacier

Pine Island Glacier (Figure 2) has received significant attention due to the ~30 km grounding line retreat along its centerline
70 (Rignot et al., 2014) (~8 km average retreat across the full width of fast-flowing trunk (Joughin et al., 2016)), ~75% increase

Field Code Changed

Field Code Changed

Deleted: (Rignot et al., 2013)

Field Code Changed

Field Code Changed

Field Code Changed

Field Code Changed

Field Code Changed

Deleted: ICESat-1

Deleted: single

Deleted: /

Deleted: Figure 2

Field Code Changed

in surface velocity (Mouginot et al., 2014) and >100 m of thinning (Bindschadler, 2002; Pritchard et al., 2009) since the 1970s, with accelerated retreat beginning in the 1990s, likely due to increased ocean heat content, circulation, and basal melt (Jacobs et al., 2011).

Total discharge across the main PIG grounding line increased from ~73 Gt/yr in the mid-1990s to ~114 Gt/yr in 2009 (Mouginot et al., 2014), with a corresponding increase from ~10 to ~12 Gt/yr across the grounding line of the South PIG ice shelf (e.g., the "Wedge" catchment of Medley et al. (2014)). Retreat, speedup and thinning peaked between 2009 and 2010, followed by an observed ~2–3% velocity decrease over the main PIG ice shelf between 2012 and 2013 (Christianson et al., 2016; Mouginot et al., 2014), and return to ~2009 velocities by early 2015. Recent inventories suggest that PIG accounts for nearly ~20% (~120–130 Gt/yr) of present-day West Antarctic discharge and ~40% (40 to 50 Gt/yr) of recent ASE mass loss (Medley et al., 2014; Mouginot et al., 2014; Rignot, 2008). This ice loss corresponds to a sea-level rise contribution of ~0.10–0.15 mm/yr – a substantial portion of the present-day Antarctic Ice Sheet contribution of ~0.2–0.4 mm/yr (Bamber et al., 2018; Church et al., 2013; Rietbroek et al., 2016; The IMBIE team, 2018; WCRP Global Sea Level Budget Group, 2018).

A detailed understanding of the processes (e.g., ocean forcing, marine ice sheet instability) responsible for these observed changes, and their relative importance over time, is critical for future projections of PIG dynamics, mass loss, and contributions to global sea-level rise.

1.1.1 Geographic setting

The fast-flowing portion of the PIG ice shelf ("main shelf", Figure 3) is ~25 km wide and nearly 100 km long, with ice thickness of ~1–1.5 km near the main grounding line, and ~300–400 m near the calving front. Surface velocities over the main shelf are currently ~4 km/yr (~11 m/day), with ~2–4-km-wide shear margins that separate the main shelf from the northeast ("North shelf") and southwest ("South shelf") sectors of the PIG ice shelf (Figure 3). In general, surface velocity is relatively slow (<100–500 m/yr) over the North and South shelves, except for a fast-flowing tributary of the South ice shelf with velocity of ~1 km/yr and thickness of ~1 km near the grounding line (Figure 2). Total ice shelf area in recent decades varied from ~5500 to ~6000 km², due to changes in the grounding line and calving front positions. The PIG catchment (Figure 2A) covers ~1.8–2.0x10⁵ km² with annual surface mass balance (SMB) estimates of ~68±6 Gt/yr (Medley et al., 2014). The surface of the PIG ice shelf is characterized by a series of longitudinal (approximately along-flow) ridges/troughs near the centerline and transverse (cross-flow) ridges/troughs toward the lateral margins that correspond to basal keels/channels (Vaughan et al., 2012) (Figure 3).

The sub-shelf bathymetry shows a large transverse seabed ridge (TSR) with relief of ~400 m above the adjacent seafloor (Figure 2B and S1). This ridge has been the site of intermittent grounding since the mid-1940s (Smith et al., 2016), and it affects circulation within the cavity, effectively blocking some of the deep, warm CDW from entering the inner cavity (De Rydt et al., 2014; Dutrioux et al., 2014b). We further subdivide the main ice shelf into "inner" and "outer" regions relative to the transverse seabed ridge (Figure S1).

Deleted: –

Deleted: from ~

Deleted: –

Field Code Changed

Field Code Changed

Deleted: (Bamber et al., 2018; Church et al., 2013; Rietbroek et al., 2016; WCRP Global Sea Level Budget Group, 2018)

Deleted: M

Deleted:

Deleted: Figure 2D

Deleted: (Figure 2C)

Deleted: . Two additional ice shelves are located to the

Deleted: of the main shelf

Formatted: Highlight

Deleted: Figure 2D

Deleted: , separated by ~2–4-km-wide shear margins

Deleted: and ice thickness are

Deleted: small

Deleted: and <300–700 m, respectively

Deleted: Figure 2

Deleted: between

Deleted: –

Deleted: full

Deleted: Figure 2

Deleted: ¶

Deleted: PIG shelf

Deleted: Figure 2D

Deleted: Figure 2

Deleted: Figure

135 The "ice plain" (e.g., Thomas et al., 2004) mentioned throughout the text describes a region over the inner [ice](#) shelf with relatively smooth, gently sloping bed (Figure S1). The lightly grounded "ice plain" was the site of significant grounding line retreat from ~1990s to ~2008, with average rates of ~1 km/yr (Park et al., 2013; Rignot et al., 2014). Our DEM record begins near the end of this retreat, when the "ice plain" region was afloat except for a few isolated grounded spots (Joughin et al., 2016).

Deleted: progressive

Field Code Changed

1.1.2 Oceanographic setting

140 Westerly surface winds near the continental shelf edge drive northward Ekman transport of surface water away from the continent. This draws deep, relatively warm CDW onto the continental shelf where it flows toward Pine Island Bay along two broad bathymetric troughs carved by previous glacial advances (e.g., Jakobsson et al., 2012; Kirshner et al., 2012).

The circulation pathway beneath the PIG ice shelf is less certain, but should generally be clockwise in nature, with modified CDW inflow at depth along the north side of the outer cavity, and outflow of relatively fresh meltwater along the south side of the outer cavity (Dutrieux et al., 2014b). Deep, inflowing water that encounters the large transverse seabed ridge is likely diverted to the south, flowing alongside the ridge within the outer cavity and moving toward the South cavity. Water at intermediate depth is expected to overtop the seabed ridge, creating a sharp density front and a northward jet at the ridge crest (De Rydt et al., 2014; Dutrieux et al., 2014b). Eventually, these waters continue down local bathymetric slopes within the inner cavity toward the grounding line. Once in the inner cavity, the dense, modified CDW reaches the grounding line (Jenkins et al., 2010), with expected cyclonic (clockwise) circulation along the main [ice](#) shelf grounding line, and fresh, buoyant meltwater outflow along the centerline and south side of the [ice](#) shelf closing the circulation loop. The temporal evolution of this general circulation pattern, and exchange between the inner, outer, and South [ice](#) shelf ocean cavities depends on a number of factors, including cavity geometry defined by the evolving ice shelf base and grounding line [position](#).

1.1.3 Previous basal melt rate assessments

155 Recent studies partition the ~2003–2008 PIG mass loss into ~65% (~95–101 Gt/yr) basal melting and ~35% (~50–62 Gt/yr) calving (Depoorter et al., 2013; Rignot et al., 2013), emphasizing the importance of basal melt for this system. Table S2 of Rignot et al. (2013) provides a comprehensive review of past basal melt rate assessments for PIG.

160 Past studies offer a general picture of PIG basal melt rate spatial distribution, with relatively high rates (>100 m/yr) near the main [ice](#) shelf grounding line and lower rates over the outer [ice](#) shelf (Bindschadler et al., 2011; Dutrieux et al., 2013; Payne et al., 2007). Little is known, however, about basal melt rate temporal variability. Bindschadler et al. (2011) concluded that transverse channels/keels formed annually near the grounding line due to seasonal variability in available ocean heat content (Thoma et al., 2008; Webber et al., 2017), while simulations by Sergienko (2013) showed that similar features may be a spontaneous byproduct of the coupled ice-shelf-plume system with constant ocean heat content.

Field Code Changed

165 2 **Data and methods**

Commented [DES1]: Input data and data processing methods

We present high-resolution surface elevation observations to investigate the spatial and temporal evolution of PIG. The following sections describe data sources and relevant processing methodology.

2.1 Elevation data

170 We use surface elevation data from a number of sources, including DEMs from satellite stereo imagery, satellite altimetry and airborne altimetry.

Deleted: stereogrammetric

Deleted: and satellite and airborne altimeters

2.1.1 WorldView/GeoEye stereo DEMs

175 We generated DEMs from very-high-resolution commercial stereo satellite imagery (DigitalGlobe WorldView-1, WorldView-2, WorldView-3, and GeoEye-1) using the NASA Ames Stereo Pipeline (ASP, (Beyer et al., 2019, 2018; Shean et al., 2016) and methodology described by Shean et al. (2016). A total of ~3000 along-track stereopairs from October 2010 to May 2015 were processed for the Amundsen and Bellinghousen Sea coastline of West Antarctica (Figure 1). For this study, we focus our analysis on a ~260x240 km region with dense WorldView/GeoEye DEM coverage covering the PIG ice shelf and lower trunk (Figure 1C).

Field Code Changed

Deleted: (Beyer et al., 2018)

Deleted: in

Deleted: West Antarctic

Deleted: Figure 1

Deleted: PIG shelf

Deleted: Figure 1

Field Code Changed

180 Stereo image dimensions are typically ~13–17 km wide and 111 km long, with ~0.3–0.5 m ground sample distance (GSD). The Level-1B (L1B) images were orthorectified using a smoothed version of the Bedmap2 surface DEM (Fretwell et al., 2013) before stereo correlation. For reference, advanced processing settings for ASP included "seed-mode 3" (sparse disp utility) to initialize the correlation, a 2-level correlation pyramid limit, a correlation timeout of 360 seconds, parabolic sub-pixel refinement, and filtering of isolated disparity map clusters with area <1024 pixels (see Shean et al., 2016 for additional details).

Deleted: P

Deleted: (see Shean et al., 2016)

185 We generated additional "cross-track" or "coincident mono" DEMs from pairs of independent mono images with geometry suitable for stereo reconstruction. We identified candidate pairs in the DigitalGlobe image archive based on the criteria in Table 1, and generated 24 DEMs from images acquired between October 2011 and January 2012. Some of these cross-track pairs were acquired on the same orbit, while others were acquired on different orbits, sometimes by different spacecraft. Final time offsets between the images ranged from 0.007 to 1.6 days.

Deleted: Table 1

190 The cross-track DEMs potentially have increased error due to horizontal displacement errors (i.e., errors due to ice flow between image acquisitions), non-ideal stereo geometry (e.g., smaller convergence angles) and the fact that some errors in ephemeris data for the two images are independent (as opposed to highly correlated errors for along-track pairs). In practice, these issues can result in increased DEM vertical/horizontal bias and increased relative error (e.g., more "tilt"). Despite potentially increased error, we include these cross-track DEMs in our analysis to fill critical gaps in coverage near the PIG grounding line, and to increase overall DEM sample size for the 2011/2012 season. As described in Section 2.2, these errors are mitigated through subsequent DEM co-registration and correction.

Deleted: residual

2.1.2 SPIRIT DEMs

We incorporated all six available SPIRIT (SPOT 5 stereoscopic survey of Polar Ice: Reference Images and Topographies, (Korona et al., 2009)) 40-m posting DEMs that covered some portion of the PIG ice shelf between January 5, 2008 and January 18, 2010. Unlike the sub-meter WorldView/GeoEye imagery, the ~5 m GSD SPOT-5 images are unable to resolve meter-scale ice sheet texture, and stereo image correlation often fails for relatively flat, featureless surfaces, leading to gaps in the output DEM. The km-scale ridges/troughs, ~100–1000 m wind-sculpted surface features, and rifts on the main PIG ice shelf, however, provide adequate texture for successful correlation. Compared to the WorldView DEMs, the SPIRIT DEMs include increased noise and additional artifacts, but cover a much larger area (~120 km swath width).

Elevation values in the SPIRIT DEMs are represented as integers, with horizontal and vertical accuracy estimates of <10 m (Bouillon et al., 2006; Korona et al., 2009), which we improve substantially using control points as described in section 2.2.1. We used the DEM V1 products (generated with correlation parameters tuned for gentle slopes), applied the corresponding "CC" mask to preserve correlation scores of 50–100% (masking most interpolated areas), reprojected to a standard Antarctic polar stereographic projection (EPSG:3031), and removed the EGM96 geoid offset to obtain elevations relative to the WGS84 ellipsoid. We filtered the resulting products to remove isolated pixels, mask elevations <20 m above sea level, and remove any pixels with >30 m absolute elevation difference from the per-pixel median of all 2010–2015 WorldView/GeoEye DEMs, effectively removing spurious DEM values associated with clouds in the original imagery.

2.1.3 Satellite and airborne altimetry

The NASA Operation IceBridge (OIB) mission collected airborne altimetry data over PIG during annual campaigns from 2009/2010 to 2014/2015, except for the 2013/2014 season. Most campaigns occurred during October–November, with data acquisition flights for a particular site typically occurring over ~1–3 days. We assembled all available NASA Airborne Topographic Mapper (ATM, (Krabill et al., 2002; Martin et al., 2012)) and Land, Vegetation, and Ice Sensor (LVIS, (Blair et al., 1999; Hofton et al., 2008)) airborne lidar data for use in our study area. A total of 25 ATM flights and 7 LVIS flights crossed the study area during the period from 2009 to 2015, with data collection for each flight typically lasting <4 hours. The high-altitude LVIS surveys on October 20, 2009 and October 10, 2011 covered a significant portion of the main ice shelf, while other LVIS/ATM flights generally consisted of a few sparse flightlines distributed across the ice shelf.

We processed all altimetry data as described by Shean et al. (2016), and produced gridded 32-m and 256-m DEMs with sparse coverage for each campaign using the ASP point2dem utility. This utility assigns the output value for each grid cell by computing the weighted mean of all points within a 1-grid-cell-width radius.

We also included available 2003–2009 NASA ICESat Geoscience Laser Altimeter System (GLAS, (Schutz et al., 2005; Zwally et al., 2002)) satellite altimetry data. These data were clustered by ~33-day campaign and gridded as described above, providing 18 additional sparse DEMs. While caution must be exercised during interpretation of these sparse data over rough surfaces or steep slopes, we included them in our analysis to extend the observational record back to 2003.

Deleted: PIG shelf

Field Code Changed

Deleted: effectively

Deleted: PIG shelf

Field Code Changed

Deleted:

Deleted: 2.2.1.2

Deleted: between

Deleted: masking

Deleted: has

Field Code Changed

Field Code Changed

Deleted: between

Deleted: -

Deleted: previously

Field Code Changed

Deleted: (Shean et al., 2016)

Deleted: ICESat-1

Field Code Changed

2.2 DEM co-registration and correction

The following sections describe a cascading co-registration and correction workflow used to improve both absolute and relative DEM accuracy over the PIG study area.

2.2.1 Co-registration with altimetry

Where possible, a point-to-point iterative closest point (ICP) algorithm (Shean et al., 2016) was used to co-register DEMs to filtered altimetry data from the sources described in Section 2.1.3. The altimetry data were queried for each DEM extent and the returned points were limited to "static" (e.g., nunataks) and "dynamic" (e.g., slow-moving ice with limited slope/roughness) control surfaces. We removed points with time offset between the altimetry point timestamp and DEM timestamp ($|t_{altimetry} - t_{DEM}| > 1 \text{ year}$). Any points over floating portions of the PIG ice shelf were excluded. The remaining points were further filtered using a maximum expected displacement (product of measured surface velocity magnitude and time offset between the point and DEM timestamp) threshold of 10 m. All control points were assumed to have vertical accuracy of $\sim 0.1 \text{ m}$ (see section 5.1 of Shean et al., 2016).

The majority of the WorldView/GeoEye DEMs had 10^6 – 10^8 filtered points available for co-registration, with $|t_{altimetry} - t_{DEM}|$ of only a few months. The ICP co-registration provided translation corrections for 368 of 575 DEMs over the PIG catchment, with a significant improvement in multiple quality metrics following co-registration (Figure 4, Table 2). Uncorrected DEMs had an initial mean vertical bias of +3.1 m above the altimetry data (Figure 4), as discussed in section 6.1.1 of Shean et al. (2016), and we applied a -3.1 m vertical correction to the remaining 207 DEMs that lacked adequate control data.

The filtered SPIRIT DEMs were co-registered with the ICP routine described in Section 2.2.1, and the results are shown in Figure S2. In addition to the filtered airborne data, a large sample of near-contemporaneous ICESat GLAS data were available for co-registration of the 2008–2009 SPIRIT DEMs. After co-registration we estimate that the lower-resolution SPIRIT DEM products have 3–4 m or better absolute vertical accuracy (1-sigma). One of the DEMs (January 3, 2009) had large residual offsets between control point and DEM elevation, and we performed a secondary round of vertical bias correction (-3.1 m) to minimize offsets between this DEM and a 2010–2015 WorldView/GeoEye DEM per-pixel median elevation composite over flat, smooth surfaces near the main ice shelf.

2.2.2 Elevation correction for ocean and atmospheric variability

After DEM co-registration, we corrected all elevation data (including altimetry) over the floating portions of the PIG ice shelf to remove the effects of ocean tides, atmospheric pressure (Inverse Barometer Effect (IBE), (e.g., Padman et al., 2003)) and mean dynamic topography.

We computed tidal amplitude Δh_t using the CATS2008A inverse barotropic tide model (an updated version of the model described by Padman et al. (2002)). The inverse barometer effect magnitude Δh_{IBE} was computed from 6-hour interval ERA-

Deleted: PIG shelf

Deleted: and maximum DEM–point time offset of 1 year

Deleted: .

Deleted: <#>WorldView/GeoEye DEM co-registration

Formatted: Normal

Deleted: <#>. Figure 3 and Table 2 show

Deleted: <#>Figure 3

Deleted: <#>Table 2

Deleted: <#>Figure 3

Deleted: <#>
<#>SPIRIT DEM co-registration

Deleted: ICESat-1

Deleted: PIG shelf

Deleted: in

Interim mean sea level pressure reanalysis data (Dee et al., 2011). We removed the 2002–2016 median pressure (985.21 hPa), and scaled residuals by ~ 1 cm/hPa to obtain the approximate inverse barometer correction. Tidal amplitude for DEM timestamps ranged from -0.75 to $+1.04$ m ($\sigma = 0.33$ m), while the inverse barometer effect amplitude ranged from -0.3 to 0.35 m ($\sigma = 0.11$ m) (Figure S3). These high-frequency (hourly–daily) corrections show good agreement with observed surface elevation records from GPS receivers on the [PIG ice shelf](#) (Shean et al., 2017).

Field Code Changed

The mean dynamic topography (Δh_{MDT}) correction removes residual offsets between the geoid and mean sea level due to ocean circulation. Estimates for mean dynamic topography near ASE are approximately -1.2 m (Andersen and Knudsen, 2009). Corrected ice surface elevation above sea level is calculated as:

Deleted: PIG shelf

Field Code Changed

$$h = h_e - \Delta h_g - \alpha (\Delta h_{MDT} + \Delta h_t + \Delta h_{IBE}) \quad (1)$$

Where h_e is measured elevation above the WGS84 ellipsoid and Δh_g is the EGM2008 geoid offset (Pavlis et al., 2012) (approximately -27.6 to -24.4 m across [PIG ice shelf](#)). To provide a smooth transition from grounded to freely floating ice, we defined the coefficient α to increase linearly with distance l downstream of the grounding line:

Deleted: PIG shelf

Deleted: W

Deleted: beyond

$$\alpha(l) = \begin{cases} 0, & l \leq 0, \\ 0.33l, & 0 < l \leq 3 \text{ km}, \\ 1, & l > 3 \text{ km}. \end{cases} \quad (2)$$

For this study, the grounding line (Figure 2 and 3) was defined with a single composite polygon derived from DInSAR (Joughin et al., 2016; Rignot et al., 2014) and high-resolution DEM data, with an approximate timestamp of 2011.

Deleted: which provides a smooth transition from floating to grounded ice for these corrections.

Deleted: Figure 2

After correction using Equation (1), surface elevation from airborne altimetry approaches 0 m above sea level over open water.

Field Code Changed

We neglect elevation change due to long-term sea level rise (~ 0.3 cm/yr) and glacial isostatic adjustment (elastic response is approximately $+2$ – 4 cm/yr for ASE (Barletta et al., 2018; Groh et al., 2012; Gunter et al., 2014)).

Deleted: (1

2.2.3 WorldView/GeoEye DEM "tilt" correction

As identified by Shean et al. (2016), a subset (~ 5 – 10%) of the WorldView/GeoEye DEMs appear to have a slight along-track and/or cross-track "tilt" of ~ 1 – 3 m over the ~ 111 km strip length, likely due to small errors in spacecraft attitude metadata. For most of these "tilted" DEMs, the available control point spatial distribution is insufficient to constrain a rigid-body ICP rotation. Initial attempts using bootstrapping and least-squares minimization of offsets between adjacent, overlapping DEMs to solve for a "tilt correction" failed due to overfitting and the propagation of larger errors near some DEM edges. To correct these problematic DEMs, we developed an optimization approach that simultaneously solved for interannual dh/dt and planar corrections to remove individual DEM tilt. In principle, this is similar to the SERAC method used for altimetry over the Greenland ice sheet (Csatho et al., 2014; Schenk and Csatho, 2012).

Deleted: in

The WorldView DEM record (November 16, 2010 to April 6, 2015) postdates the period of rapid PIG speedup that ended in ~ 2009 , and surface velocities and SMB display limited variability from 2010–2015 (Christianson et al., 2016; Shean et al., 2017). Thus, while the dynamic response to earlier rapid grounding line retreat and speedup continues to propagate upstream across the PIG catchment, we expect relatively limited variability in elevation change rates during this period.

Field Code Changed

We manually masked the main ice shelf and fast-flowing grounded ice stream within ~30 km of the grounding line, and then used the criteria listed in Table 3 to identify "dynamic control surfaces" (Figure 5) over grounded ice with limited linear trend (dh/dt) and limited residual variance about this trend. Over these surfaces, the elevation at any particular DEM pixel i (with spatial coordinates x_i and y_i) at time j is given by:

$$h_{i,j} = (a_i t_j + b_i) + (c_j x_i + d_j y_i + e_j) \quad (3)$$

where a_i and b_i represent the slope and offset of a linear model fit to elevation values at pixel i , and coefficients c_j , d_j and e_j define a planar correction for all i within a DEM at time t_j .

We solved for these coefficients using least-squares minimization with regularization and a smoothness constraint designed to penalize large spatial gradients. Elevation values from filtered, gridded altimetry data were included in the solution with increased weight. Stereo DEMs with <40 km along-track length were limited to a vertical offset correction (e_j), with no tilt correction ($c_j = d_j = 0$). Limits for tilt magnitude were increased for cross-track DEMs (Section 2.1.1) and limits for vertical offset were increased for input DEMs that were not initially co-registered using ICP. Tilt magnitude was limited in the DEM cross-track direction, as most of the observed tilt was in the DEM along-track direction. Figure 5 and Table 4 summarize the results of these corrections, with considerable improvement in all metrics.

2.2.4 Output elevation data

We prepared a resampled "stack" of all co-registered, corrected DEMs over the PIG ice shelf using a common 256-m grid. Additional stacks with increased grid resolution (64-m and 32-m, respectively) were prepared over high-priority areas such as the inner ice shelf and GPS validation sites (Shean et al., 2017)).

2.3 Post-correction DEM accuracy

As discussed by Shean et al. (2016), the uncorrected vertical/horizontal accuracy for the along-track stereo DEMs is <5.0 m. After systematic artifact removal and co-registration, vertical accuracy can be less than <0.2–0.4 m for surfaces with <10° slope. For the PIG ice shelf, we conservatively estimate the final DEM accuracy to be ~1 m after co-registration and least-squares "tilt" correction. We initially expect increased uncertainty for 2013/2014 DEMs due to reduced availability of OIB altimetry data during this season. This uncertainty, however, was reduced after the least-squares correction, which leveraged altimetry data and corrected WorldView/GeoEye DEMs from adjacent years.

Several factors can reduce the effectiveness of DEM co-registration with altimetry. The primary problems for PIG include sparse control data with limited variation in surface slope and aspect, and longer $|t_{altimetry} - t_{DEM}|$ time offsets (~1–12 months). Over these timescales, surface processes (e.g., accumulation/ablation, wind redistribution of snow) can potentially lead to surface elevation changes of ~1 m, and advection of small-scale surface features can lead to horizontal co-registration errors.

Deleted: trunk

Deleted: Table 3

Deleted: Figure 4

Formatted: Subscript

Deleted: j

Deleted: Tilt tolerances

Deleted: tolerances

Deleted: tolerance

Deleted: Figure 4

Deleted: Table 4

Deleted: PIG shelf

Deleted: (i.e.,

Deleted: in

Deleted: CE90/LE90

Deleted: PIG shelf

Deleted: between the DEM and altimetry timestamps

We used a network of five 2012–2014 GPS sites on the outer [ice shelf](#) (Shean et al., 2017) as independent check points for WorldView DEMs. Corrected DEM elevations show good agreement (~ 0.72 m root mean squared error [RMSE] and ~ 0.57 normalized median absolute deviation [NMAD]) with cm-accuracy surface elevations derived from GPS interferometric reflectometry (GPS-IR) antenna height records at each site. Unfortunately, no valid SPIRIT DEM pixels were available near the 2008–2010 GPS sites.

2.4 Annual surface elevation composites and mosaics

We generated weighted-average composites using the ASP `dem_mosaic` utility for all available elevation data in a given year (September–April, but typically October–March), with a nominal January 1 timestamp ([Figure 6](#)). For each output pixel, the weighted averaging algorithm assigns greater weight to input pixels from spatially continuous sources (e.g. DEMs with few data gaps) and penalizes isolated pixels or clusters of pixels (see ASP documentation for details). The resulting composites appear seamless, but can include smoothing artifacts due to variable temporal sampling of input elevation data, especially for features that advect in the along-flow direction.

Adjacent WorldView/GeoEye stereo [images](#) are often acquired weeks or months apart during a particular season due to clouds and/or competition for resources. Even after DEM co-registration and correction, this [asynchronous](#) sampling can introduce horizontal and vertical feature offsets between adjacent DEMs in fast-flowing regions. Generally, this [sampling](#) is not a problem for smaller targets covered by a single WorldView/GeoEye DEM footprint (e.g., Greenland outlet glacier termini). Larger targets like the [PIG ice shelf](#), however, require >10 WorldView/GeoEye DEMs for complete coverage, and more sophisticated mosaicking approaches are necessary to preserve local features.

To obtain full [ice shelf](#) coverage while also preserving timestamps and relative elevation values within individual input DEMs, mosaics without averaging or blending were generated for the \sim October–March period each year. We used a "reverse" ordering scheme for input DEM timestamps, so that the last DEM from each season was mosaicked on top. Finally, we generated WorldView/GeoEye DEM mosaics when complete [ice shelf](#) coverage was available over a relatively short time span (e.g., October–December 2012, [Figure 3](#)). In such cases, input DEM products were manually selected and ordered to minimize feature offsets.

2.5 Surface velocity

Surface velocity data constrain horizontal [ice shelf](#) advection rates and aid interpretation of observed elevation change. In an effort to generate self-consistent velocity and DEM products, we estimated velocity using feature tracking with normalized cross-correlation of two DEMs, similar to the approach described by Dutrieux et al. (2013). However, this approach is susceptible to spurious correlations and data gaps over flat, featureless areas, especially for low-resolution inputs (e.g., 40-m SPIRIT DEMs). This technique also fails for longer time intervals (>2 years), as surface processes, deformation, rotation due to velocity gradients, and spatially variable basal melt decreased coherence. For these reasons, we used an independent set of

Deleted: Figure 5

Deleted: DEMs

Deleted: temporal

Deleted: PIG shelf

Deleted: -

Deleted: -wide

Deleted: Figure 2D

Deleted: -

Deleted: and

gridded velocity products, which enabled reconstruction of particle paths for arbitrary elevation data, including sparse altimetry.

420 We ~~compiled~~ 22 surface velocity mosaics (Christianson et al., 2016; Joughin, 2002; Joughin et al., 2010) from TerraSAR-X/TanDEM-X, Advanced Land Observing Satellite (ALOS) Phased Array type L-band Synthetic Aperture Radar (PALSAR) and Landsat-8 (LS8) data (Figure 2C). The 500-m ALOS and LS8 products cover the entire PIG ice shelf during late 2006, 2007, 2008, 2010, 2013, 2014, and 2015, while the 100-m TSX/TDM products are available every ~3–6 months over the main ice shelf from 2009–2015.

425 We derived spatially and temporally continuous velocity fields for the full PIG ice shelf using piecewise linear interpolation via 3-D (x,y,t) Delaunay Triangulation. Linear barycentric interpolation was then used to extract spatially continuous velocity grids with 512-m resolution for a regular time interval of 122 days from January 1, 2008 to June 1, 2016. The interpolated velocity products were smoothed in the time dimension with a 610-day, 2nd-order Savitzky-Golay filter, and then in the spatial dimension with a 2.5-km rolling median filter to mitigate artifacts in the input mosaics. To obtain velocity fields with increased
430 spatiotemporal sampling, we performed secondary interpolation with a high-resolution timestep (e.g., 5–20 day) and increased spatial sampling (e.g., 32–256 m), with a final Gaussian smoothing filter (~0.17-km sigma) applied in the spatial dimension to reduce any residual interpolation artifacts. The basal melt rate calculations described in Section 3.2 required estimates of the velocity divergence, which we calculated from these interpolated, smoothed velocity products for each high-resolution time step using a central-difference approach.

435 2.6 Bed topography

We evaluated five different bed datasets for PIG (Figure S1), including Bedmap2 (Fretwell et al., 2013), an aerogravity inversion constrained by Autosub bathymetric data (De Rydt et al., 2014; Dutrieux et al., 2014b), an aerogravity/Autosub inversion constrained by active-source seismic surveys (Muto et al., 2016), a mass-conserving bed embedded in Bedmap2 (Morlighem et al., 2011), and the CReSIS L3 gridded Multichannel Coherent Radar Depth Sounder (MCoRDS) ice thickness
440 product from 2009–2010 airborne radio echo sounding. The extent and resolution of these products is variable, with significant elevation differences (>100–300 m) in places, especially over the PIG inner cavity (Figure S1).

We produced a new combined bed dataset (Figure S1C) using aerogravity/Autosub data, existing open-water bathymetry, and all available quality-controlled CReSIS MCoRDS and British Antarctic Survey (BAS) Polarimetric Airborne Survey Instrument (PASIN) ice thickness measurements collected over grounded ice. We used "anisotropic interpolation" to fit a smooth surface to these data using an inversion procedure that preferentially minimizes bed curvature in the along-flow direction, while matching the bed elevation at data points to within the estimated data errors (see methods of Medley et al.,
445 2014; Mueller et al., 2012). While some local "peaks" over the longitudinal seabed ridge beneath the PIG ice shelf may be biased high, this bed appears most consistent with observed recent grounding line evolution (Joughin et al., 2016).

Deleted: used

Field Code Changed

Deleted: Figure 2

Deleted: 500 m/px

Deleted: PIG shelf

Deleted:

Deleted: /px

Deleted: The mosaics were derived from images acquired over a ~11–189 day period, with most spanning <88 days.

Deleted: PIG shelf

Commented [DES2]: with the `scipy.interpolate.LinearNDInterpolator`

Deleted: s

Field Code Changed

Field Code Changed

Field Code Changed

Deleted: (see methods of Medley et al., 2014)

Deleted: PIG shelf

Field Code Changed

2.7 Surface mass balance (SMB)

The Regional Atmospheric Climate Model (RACMO) v2.3 (Ettema et al., 2009; Lenaerts et al., 2012; Van Meijgaard et al., 2008; Van Wessem et al., 2014) provides continent-wide estimates of surface mass balance on a 27-km grid. To estimate SMB over the [PIG ice shelf](#), we used monthly average SMB products available through December 2013, and repeated the observed 2013–2014 SMB signal for calculations spanning 2014–2015. We generated gridded RACMO SMB products with the same extent and spatial sampling as the DEM and velocity products [using bicubic interpolation](#).

Field Code Changed

Deleted: PIG shelf

Deleted: The

Deleted: data

Deleted: were interpolated over the study area to generate gridded products ...

Formatted: Heading 1

3 Elevation change and basal melt rate derivation

We consider elevation change for PIG using both Eulerian dh/dt (fixed reference grid) and Lagrangian Dh/Dt (grid moving with the surface) descriptions. These two approaches are complementary and provide distinct information over grounded and floating ice.

Formatted: Heading 2

3.1 Theory

Assuming incompressibility, constant ice density, and column-average velocity \mathbf{u} , the Eulerian description of mass conservation for a column of ice with ice-equivalent thickness H can be expressed as:

Deleted: (after removing firm-air content d)

$$\frac{\partial H}{\partial t} = -\nabla \cdot (H\mathbf{u}) + a - b \quad (4)$$

where a is [surface mass balance](#) (meters ice equivalent for time interval dt) and b is basal melt rate (meters ice equivalent, defined as positive for melt).

Deleted: surface accumulation rate

The flux divergence term, $\nabla \cdot (H\mathbf{u})$, can be expanded as:

$$\nabla \cdot (H\mathbf{u}) = H(\nabla \cdot \mathbf{u}) + \mathbf{u} \cdot (\nabla H) \quad (5)$$

where $\nabla \cdot \mathbf{u}$ is the velocity divergence (positive for extension) and ∇H is the thickness gradient.

The relationship between Lagrangian (denoted by material derivative operator $\frac{D}{Dt}$) and Eulerian thickness change is provided by the material derivative definition:

$$\frac{DH}{Dt} = \frac{\partial H}{\partial t} + \mathbf{u} \cdot (\nabla H) \quad (6)$$

Equations 4, 5, and 6 can be combined to obtain Lagrangian thickness change for the column:

$$\frac{DH}{Dt} = -H(\nabla \cdot \mathbf{u}) + a - b \quad (7)$$

Over grounded ice, we assume that the bed elevation remains constant, and can substitute Eulerian surface elevation change dh/dt for Eulerian thickness change dH/dt . This assumption does not hold for floating ice. If we assume hydrostatic equilibrium, however, we can estimate freeboard ice thickness from observed surface elevation. We remove firm-air content d from observed

surface elevation h to obtain ice-equivalent freeboard surface elevation, and then compute ice-equivalent freeboard thickness

H_f :

$$H_f \approx (h - d) \left(\frac{\rho_w}{\rho_w - \rho_i} \right) \quad (8)$$

assuming a constant density for sea water (ρ_w) and ice (ρ_i). This ice-equivalent freeboard thickness H_f can then be substituted for H in Equation 7. We assume that any changes in d , ρ_w , and ρ_i are negligible during our study period, so the DH_f/Dt term reduces to Lagrangian surface elevation change (Dh/Dt), resulting in a modified mass-conservation expression for a column of floating ice;

$$\frac{Dh}{Dt} = -(h - d)(\nabla \cdot \mathbf{u}) + (a - b) \left(\frac{\rho_w - \rho_i}{\rho_w} \right) \quad (9)$$

3.2 Eulerian long-term interannual trend

To characterize long-term (~5–10 year) elevation change over the PIG ice shelf during and after the period of rapid grounding-line retreat, we computed interannual per-pixel trends for the 2003–2010 and 2010–2015 periods. These trends were determined using a linear fit to surface elevation for each grid cell with 3 or more observations, with >6 valid samples available for most cells. No smoothness constraint was imposed – all fits were computed independently, although adjacent elevation values are highly correlated.

3.3 Basal melt rate

Both Eulerian and Lagrangian frameworks can be used to estimate the basal melt rate. The Lagrangian description tracks elevation change for the same column of ice over time, eliminating potential aliasing due to advection of high-frequency surface gradients (i.e., ice shelf surface ridges and troughs). If velocity divergence and surface mass balance are known, Equation 9 can be rearranged to solve for the component of observed elevation change due to basal melt:

$$b = - \left(\frac{Dh}{Dt} + (h - d)(\nabla \cdot \mathbf{u}) \right) \left(\frac{\rho_w}{\rho_w - \rho_i} \right) + a \quad (10)$$

3.4 Basal melt rate implementation

Past studies of basal melt rate using a Lagrangian framework used *in situ* observations (e.g., Jenkins et al., 2006), a single pair of gridded DEM observations (e.g., Dutrieux et al., 2013), or a series of sparse altimetry data (e.g., Moholdt et al., 2014). The approach presented here uses hundreds of independent DEM observations with variable spatial coverage over an 8-year time period. This set of DEMs provides thousands of combinations for basal melt rate computation, with the flexibility to vary the time interval Dt . Most of the PIG ice shelf DEM data were acquired seasonally from ~October–March, so we computed interannual Dh/Dt for time intervals of ~1 and ~2 years. Longer time intervals decrease spatial resolution, as the observed

Formatted: Font: Italic

Formatted: Font: Italic, Subscript

Deleted: H

Deleted: Equation 8

Formatted: Font: Italic

Deleted: into

Deleted: to obtain a mass-conservation expression for Lagrangian surface elevation change for the floating ice, dropping the constant d from the material derivative term

Formatted: Heading 2

Deleted: PIG shelf

Deleted: -

Deleted: surface accumulation

Deleted: Lagrangian Dh/Dt b

Formatted: Heading 2

Deleted: Lagrangian Dh/Dt

Deleted: s

Formatted: Font: Not Italic

Field Code Changed

Deleted: Lagrangian Dh/Dt

Deleted: PIG shelf

530 Dh/Dt values are integrated across a longer path, but they provide improved signal-to-noise ratio for Dh/Dt , and we use the ~2 year products for further analysis.

To calculate basal melt rate, we track each pixel in an earlier DEM acquired at time t_i (DEM_i) to its corresponding downstream location where it intersects a later DEM acquired at time t_j (DEM_j). Since our velocity fields vary over time (Section 2.5), an appropriate time step Δt for this tracking is automatically determined based on the grid cell size and maximum velocities (e.g., ~10–20 days for 256-m grid). For each time step n $\{n \mid 0 < n \leq Dt/\Delta t, n \in \mathbb{Z}^+\}$, all valid pixels ("particles") from DEM_i are
535 propagated along flow paths (Figure 7) computed from the time-variable velocity fields. This propagation yields updated DEM_i particle positions at time $(t_i + n\Delta t)$. For those particles whose paths intersect DEM_j , we calculate the observed Lagrangian elevation change rate as:

$$\frac{Dh}{Dt} = \frac{h_j - h_i}{t_j - t_i} \quad (11)$$

The observed cumulative particle Dh/Dt is then used to estimate evolving surface elevation h at each time step n along the particle path (assuming the Dh/Dt rate is constant), and local velocity divergence $(\nabla \cdot \mathbf{u})$ values are sampled at each time step
540 n along the particle path from the continuous velocity products described in Section 2.5. The corresponding local $h(\nabla \cdot \mathbf{u})$ is then integrated over the full path:

$$h(\nabla \cdot \mathbf{u}) \approx \frac{\sum_{n=0}^{Dt/\Delta t} (h_i + n\Delta t \frac{Dh}{Dt}) (\nabla \cdot \mathbf{u})_n}{Dt} \quad (12)$$

This approach should accurately capture time-variable thinning/thickening due to local velocity divergence experienced along each path, rather than sampling velocity divergence from single, fixed velocity grid. We also sampled time-variable SMB grids at each time step, but the spatiotemporal variability for the monthly 27-km products is limited along the ~8 km particle paths,
545 and we used a time-averaged estimate for α extracted at the particle path midpoint. Finally, we substituted the cumulative particle Dh/Dt and local $h(\nabla \cdot \mathbf{u})$ into Equation 10, which provides an integrated basal melt rate estimate for a single pixel across a single pair of DEMs.

3.5 Basal melt rate path distribution

We consider two end members for the spatiotemporal distribution of ice shelf basal melt rates. End member #1 assumes a
550 fixed, 3D "melt rate field" in the ocean cavity beneath the PIG ice shelf that varies spatially but not temporally, so that features with variable draft (i.e., keels and channels) melt at different rates as they advect through this field. End member #2 assumes that melt rate spatial variability is highly correlated with local ice shelf thickness gradients (and associated basal slope), so that local melt rates advect with features on the ice shelf (e.g., once formed, a transverse basal channel will continue to melt at a similar rate as it advects downstream). In reality, basal melt rates are likely sensitive to some combination of these two end-member scenarios.

The methodology described in Section 3.4 provides basal melt rate estimates for each particle in a Lagrangian reference frame. For subsequent analysis on a regular grid, we must remap these observations into a common, global Eulerian reference frame.

Deleted: Figure 6

Deleted: in practice,

Deleted: particle

Deleted: from

Formatted: Heading 2

Deleted: horizontally and vertically variable

Deleted: does not vary over time

Deleted: rapidly

565 This step is complicated by the fact that the long time intervals between DEM observations (~2 years) and high advection rates (~4 km/yr) on the main **PIG ice shelf** result in particle path lengths (~8 km) that greatly exceed the input DEM grid cell size and the desired melt rate grid cell size (256 m). To address this issue and to evaluate the two basal melt rate end-member scenarios, we developed two approaches to work with basal melt rates from Lagrangian Dh/Dt measurements in an Eulerian reference frame: "along-flow distribution" and "initial-pixel" (Figure 7).

570 3.5.1 Along-flow distribution

The "along-flow distribution" approach partitions observed particle basal melt rates (Section 3.4) evenly across each path, and computes statistics for each cell in a fixed Eulerian grid using all paths that pass through that cell (Figure 7). This approach potentially provides a more realistic map of the melt rate "field" (end member #1), but it effectively smooths basal melt rate estimates in the along-flow direction, especially for longer path lengths. This leads to reduced resolving power for local basal melt rate spatial variability (end member #2), especially for features with transverse orientation (e.g. transverse channels/keels, rifts).

575 The path history of all valid particles for a particular DEM_i-DEM_j combination is reduced to identify a unique set of occupied grid cells in the global Eulerian reference frame. For each particle path, basal melt rate b is calculated as described in Section 3.4 and these values are distributed evenly along encountered cells. This procedure yields a spatially variable particle count within each cell in the global Eulerian coordinate system; only one particle will pass through a cell on the upstream edge of the domain, while ~10–100 particles could pass through a cell near the center of the domain over the full Dt interval. We then compute the median and NMAD for each cell (Figure 7). This approach reduces noise and provides metrics to evaluate variance and uncertainty in derived basal melt rates.

585 3.5.2 Initial-pixel

The "initial-pixel" approach assigns particle basal melt rate values to the corresponding path origins in DEM_i , so the resulting basal melt rates grids have the same spatial extent as DEM_i . This approach is relatively straightforward, and was used in earlier work (e.g., Dutrieux et al., 2013). It preserves the relative spatial distribution of basal melt rates across individual features in DEM_i (e.g., channels and keels), but doesn't resolve where along the ~8 km particle path that melt actually occurred.

590 For a given DEM_i-DEM_j combination, the initial-pixel approach assigns particle basal melt rate values to DEM_i pixel locations. For each initial DEM_i , we then create stacks of available DEM_i-DEM_j initial-pixel basal melt rate products and compute a per-pixel stack median map. In other words, basal melt rates calculated from each valid downstream DEM_j are assigned to the initial DEM_i pixel locations, and median values for each DEM_i pixel are computed assuming no temporal variability in basal melt rates for all valid t_i-t_j intervals.

Deleted: PIG shelf

Deleted: observed Lagrangian Dh/Dt

Moved (insertion) [2]

Deleted: Figure 6

Deleted: We present results for both approaches and evaluate the two melt-rate end-member scenarios.

Formatted: Heading 3

Deleted: products

Deleted: Figure 6

Deleted: unique

Deleted: Figure 6

Formatted: Heading 3

Deleted: products

Deleted: to evaluate end member scenario #2

605 3.5.3 Path distribution considerations

Under melt-rate end-member #1, the initial-pixel approach will introduce a negative bias for a fixed basal melt rate field with relatively large negative spatial gradient (e.g., 200 m/yr to 100 m/yr over 8 km in the inner cavity), as the mean path basal melt rate (150 m/yr) will be assigned to the initial-pixel locations (where rates are locally 200 m/yr). We experimented with an approach using path mid-point locations rather than initial-pixel locations, but this resulted in large gaps near the grounding line and prevented direct comparison of basal melt rates with the original DEM_i elevations. Under melt-rate end-member #2, the initial-pixel approach provides more realistic basal melt rate magnitude and spatial distribution than the along-flow distribution approach. The difference between the two approaches will be negligible for areas of the [PIG ice shelf](#) with low surface velocity (<250 m/yr).

3.6 Basal melt rate composites

615 In the above sections, we described basal melt rate calculations for a single DEM_i-DEM_j combination with sufficient overlap and a t_i-t_j time interval that falls within the chosen Dt range (~2 years), which represents only one of many potential valid DEM_i-DEM_j combinations that can be formed from the full set of DEMs over the [PIG ice shelf](#).

For a given DEM_i , after we calculate basal melt rates using the first viable DEM_j , the DEM_i particles are further propagated and the process is repeated for all other viable DEM_j until the t_i-t_j time interval exceeds the maximum Dt interval. The entire process is then repeated for all possible DEM_i .

620 For our chosen Dt of ~2 years, a total of 117 unique DEM_i with initial t_i timestamps spanning 2008–2013 and sufficient DEM_j intersection area were available over the [PIG ice shelf](#). Each DEM_i formed ~2–40 valid DEM_i-DEM_j combinations, yielding a final set of >1000 independently generated DEM_i-DEM_j basal melt rate products.

625 The individual DEM_i-DEM_j basal melt rate products can have relatively high uncertainty and/or limited spatial extent, so we created annual melt-rate mosaics and composites to reduce noise and increase total spatial coverage. We used different methodology for the "along-flow distribution" and "initial-pixel" approaches, as described below.

3.6.1 Along-flow distribution composites

630 We generated weighted-average basal melt rate composites from individual "along-flow distribution" basal melt rate products. This approach provides basal melt rate grids centered on January 1 for the ~2-year interval products. For each grid cell in the output mosaics, the weighted-average approach favors pixels near the center of input products with larger areal coverage. Per-pixel standard deviation is also calculated for each ~2-year basal melt rate composite, providing maps that capture the spatial distribution of basal melt rate uncertainty (and any true basal melt rate temporal variability during the ~2-year period). The annual composites were then used to generate a mean basal melt rate composite for the full 2008–2015 period.

Formatted: Heading 3

Deleted: PIG shelf

Moved up [2]: We present results for both approaches and evaluate the two melt-rate end-member scenarios.

Deleted:

Formatted: Heading 2

Deleted: Shelf-wide b

Deleted: PIG shelf

Deleted: PIG shelf

Formatted: Heading 3

3.6.2 Initial-pixel mosaics

The per-pixel stack median products described in Section 3.5.2 provide high-resolution maps of local basal melt rates, but they are limited to the *DEM_t* spatial extent. To overcome this limitation, we generated mosaics of the stack median products using a reverse time-ordering scheme, so basal melt rate estimates for the most recent *DEM_t* timestamp were mosaicked on top. This approach preserves the local basal melt rate distribution within each stack median product, while providing coverage over as much of the ice shelf as possible, with limited time offset between spatially adjacent observations. These products can be directly compared with surface elevation (and corresponding freeboard thickness estimates) from the reverse-time-order *DEM* mosaics described in Section 2.4.

3.7 Uncertainty and sources of error

Surface elevation uncertainty over the *PIG ice shelf* includes errors due to the geoid model (~ 0.1 – 0.4 m), mean dynamic topography (~ 0.2 m), and tide/IBE correction (~ 0.1 m). For simplicity, we assume a constant firn-air content of 12 m with uncertainty of ± 2 m to account for any spatial and temporal variability (see Appendix of Shean, 2016). We used a depth-averaged density for ice and underlying ocean water of 917 ± 5 kg/m³ and 1026 ± 1 kg/m³, respectively, and assume that these densities are constant in both space and time. We assume uncorrelated errors of 1 m for surface elevation, 50 m for bed elevation, 30 m/yr for velocity (for $\sim 37.5^\circ$ look angle and ± 0.5 m tide) (Joughin, 2002) and 28% for SMB (Depoorter et al., 2013).

Our conversion from surface elevation to ice thickness assumes that the ice shelf is in hydrostatic equilibrium (Shean et al., 2017). We use a consistent methodology and the same assumptions of hydrostatic equilibrium for the full 2008–2015 study period, which increases confidence in observed temporal change. We do not update the grounding line mask for basal melt rate calculations, and some of the persistent high and low basal melt rate values < 1 – 2 km downstream of the grounding line may be related to evolving grounding line position and insufficient masking over grounded ice (Joughin et al., 2016; Milillo et al., 2017). Transient regrounding of keels will yield increased surface elevations and larger apparent freeboard thickness values. This may also lead to localized ice deformation and non-zero vertical strain rates that are inconsistent with the assumption that surface velocity equals the column-average velocity.

Uncertainty for elevation change and basal melt rate products depends on the time interval. For example, assuming that errors are uncorrelated, a 1-m absolute error in surface elevation should result in ~ 1.4 m combined error in elevation change. This elevation change uncertainty should remain constant, so integrating observations over longer periods will result in greater signal-to-noise for annual elevation change rates (e.g., ~ 1.4 m/yr error for a 1-year interval or ~ 0.7 m/yr for a 2-year interval, assuming constant rates). This estimate does not, however, include slope-dependent vertical error due to cumulative horizontal displacement error, which will increase for longer time intervals. It is challenging to quantify this Dh/Dt uncertainty contribution in a forward sense, as multiple sources (e.g., cumulative displacement error from velocities, DEM co-registration, DEM resampling) can lead to slope- and aspect-dependent errors. Basal melt rate products can also include artifacts over shear

Formatted: Heading 3

Deleted:

Deleted: "

Deleted: "

Deleted: ing

Deleted: PIG shelf

Field Code Changed

Field Code Changed

Deleted: time

Field Code Changed

Deleted: root-mean-square

Deleted: uncertainty

margins and near the ice front due to anomalously large Dh/Dt values ($\pm 20\text{--}40$ m) from advection of near-vertical surface gradients (e.g., ice front, icebergs, rifts) and errors in velocity divergence.

The stacking and averaging approaches described in Section 3.6 should reduce many of these errors, but this improvement is difficult to capture with formal error estimates. The initial-pixel stack per-pixel NMAD (Section 3.5.1) and along-flow per-pixel standard deviation (Section 3.6.1) metrics can provide maps of uncertainty, but these estimates will also include any true basal melt rate temporal variability during the observation period.

4 Results

4.1 Long-term Eulerian elevation change

Figure 8 shows long-term Eulerian elevation change (dh/dt) for the full study area. From 2003 to 2010, thinning rates <30 km upstream of the grounding line were $\sim 5\text{--}10$ m/yr, while those farther upstream over the catchment were ~ 1 m/yr. From 2010 to 2015, thinning rates near the grounding line decreased to $\sim 0\text{--}1$ m/yr, with increased thinning of $\sim 1\text{--}2$ m/yr over the catchment. Thinning rates also increased to $\sim 3\text{--}4$ m/yr over upstream ice stream shear margins within ~ 60 km of the grounding line, especially the north shear margin.

A series of curvilinear elevation anomaly "bands" with orientation approximately transverse to flow is apparent over the catchment $\sim 40\text{--}100$ km upstream of the grounding line (Figure 8D). These features are related to dense series of arcuate surface crevasses (e.g., Scott et al., 2010) that display elevation change due to advection. Individual DEMs show elevation differences of ~ 0.5 m between these crevasse bands and inter-band surfaces.

Over the PIG ice shelf, we observe 2010–2015 dh/dt signals with spatial scales of $\sim 10\text{--}15$ km that are unrelated to advection of km-scale surface features (Figure 8D). We observe $\sim 1\text{--}2$ m/yr thickening downstream of the grounding line on the north side of the inner main ice shelf and ~ 1 m/yr thinning over the south side of the outer main ice shelf. The South PIG ice shelf shows <1 m/yr thinning from 2010–2015, with ~ 3 m/yr thinning over upstream ice within ~ 10 km of the grounding line. The North ice shelf shows little elevation change with $<0.5\text{--}1$ m/yr thinning upstream of the grounding line.

4.2 Basal melt rate spatial distribution

Figure 9 shows mean 2-year basal melt rate products for the 2008–2015 period. Full ice shelf basal melt rates were ~ 82 Gt/yr for "initial-pixel" and ~ 93 Gt/yr for "along-flow distribution" composite 2-year products.

In general, basal melt rates are $>150\text{--}200$ m/yr near the main ice shelf grounding line, with highest rates of >250 m along the north side of the grounding line (Figure S4). Basal melt rates are generally $\sim 50\text{--}100$ m/yr over the main ice shelf inner cavity, where ice thickness exceeds $\sim 600\text{--}700$ m, and $\sim 10\text{--}30$ m/yr over most of the outer ice shelf, where ice thickness is $\sim 300\text{--}500$ m. We observe considerable anisotropy, with longitudinal spatial correlation over lengths scales of ~ 20 km and significant transverse \sim km-scale variability. This is true for both the "initial-pixel" and "along-flow distribution" products (Figure 9), suggesting that this anisotropy is not a result of smoothing in the along-flow direction. The northern third of the outer main ice

Deleted: Figure 7

Deleted: -

Deleted: -

Deleted: We also note

Deleted: significantly increased 2010–2015 thinning rates ($\sim 3\text{--}4$ m/yr) ...

Deleted: Figure 7

Deleted: during the 2010–2015 period

Deleted: PIG shelf

Deleted: Figure 7

Deleted: PIG shelf

Deleted: upstream

Deleted: Figure 8

Deleted: Lagrangian Dh/Dt

Deleted: -

Deleted: Figure 8

shelf displays ~3–4 longitudinal features with elevated basal melt rates of ~30–40 m/yr (red arrow in [Figure 9](#)). Upstream of these features, a broad (~10 km wide x 20 km long) region of low-relief transverse ridges/troughs displays reduced basal melt rates of ~5–10 m/yr (green arrow).

Deleted: Figure 8

Basal melt rates are ~0–10 m/yr over the South [ice shelf](#) and ~0–5 m/yr over the North [ice shelf](#) ([Figure 9](#)). High basal melt rates of ~60–90 m/yr are observed near the relatively deep (~900 m) grounding line of the fast-flowing (~0.7–1.0 km/yr) South [ice shelf](#) tributary. Elevated basal melt rates of ~20–50 m/yr are also observed within large channels on the [South ice shelf](#) (blue arrow in [Figure 9](#)). Integrated basal melt rates over the North and South [ice shelves](#) are ~5 and ~10 Gt/yr, respectively.

Deleted: Figure 8

Deleted: s

Deleted: Figure 8

735 4.3 Channel-scale melt distribution

We used the "initial-pixel" basal melt rate mosaics to evaluate observed basal melt rates for basal channels and keels on the [Main ice shelf](#). We applied a high-pass filter (1.5 km sigma Gaussian) to annual "reverse" order DEM mosaics (Section 2.4), and defined masks for channels and keels using filtered elevations less than -1 m and greater than +1 m, respectively ([Figure 10 and S5](#)). These masks were applied to corresponding 2-year "initial-pixel" basal melt rate products, and weighted-average composites were generated from all available years to document the spatial distribution of main [ice shelf](#) channel and keel melt rates for the 2008–2015 period. The value at any given pixel in the channel (keel) composite is derived from melt rates for several advecting channels (keels) that intersected that pixel over time, providing a sample of background melt rates ([end member #1 in Section 3.5](#)) for channel (keel) features at different locations in the cavity.

Deleted: m

Deleted: Figure 9

Deleted: full

The highest basal melt rates are associated with longitudinal surface ridges (basal keels) within ~3–4 km of the grounding line.

In the inner cavity (~4–15 km from the grounding line), high basal melt rates (>100 m/yr) are associated with both longitudinal surface troughs (basal channels) and surface ridges (basal keels). Several persistent channels display high basal melt rates throughout the 2008–2015 record, but there is more apparent temporal variability associated with deep keels due to grounding and ungrounding.

Deleted: between

Over the mid to outer [ice shelf](#), we observe relatively high basal melt rates [on keels](#) (~20–40 m/yr) and limited basal melt rates in transverse channels (~0–10 m/yr). Both channels and keels display higher basal melt rates over the northern portion of the outer [ice shelf](#) (red arrow in [Figure 9](#)). Higher basal melt rates of ~10–20 m/yr are observed over ~50–70 km-long longitudinal keels near the [ice shelf](#) centerline, while ~0 m/yr basal melt rates are observed within adjacent longitudinal channels. One prominent longitudinal keel displays basal melt rates of ~30–40 m/yr (black arrow in [Figure 9](#)).

Deleted: over

Deleted: We note that b

Deleted: Figure 8

Deleted: Figure 8

5 Discussion

755 5.1 Long-term elevation change

Grounding line retreat and speedup through 2010, combined with inherent marine ice sheet instability, are primarily responsible for the strong thinning observed upstream of the grounding line at PIG (Joughin et al., 2010). Our observations show that this thinning decreased after 2010 ([Figure 8](#)), which is consistent with results from model simulations documenting

Deleted: (Figure 7)

the inland migration of the associated speedup (Joughin et al., 2010). The end of rapid grounding line retreat and the regrounding of deep keels on the transverse seabed ridge (Christianson et al., 2016; Joughin et al., 2016) likely contributed to decreased thinning rates immediately upstream of the grounding line after 2010. The continued thinning over upstream shear margins (Figure 8) can also be attributed to this evolution, as sustained thinning rates of >5–10 m/yr over the main trunk prior to 2010 (Flament and Rémy, 2012; Joughin et al., 2010; Wingham et al., 2009) led to an increase in surface slopes and transverse driving stress across the shear margins.

5.2 Basal melt rate spatial distribution

Our results show a ~11 Gt/yr difference between the full ice shelf along-flow distribution and initial-pixel basal melt rate estimates, with most of this difference over the inner cavity. This discrepancy is likely related to large spatial gradients in the "fixed" melt rate field (end member #1), which we would expect to introduce a negative bias in the initial-pixel basal melt rate estimates, as described in Section 3.5. Thus, the along-flow distribution melt-rate of ~93 Gt/yr estimate is likely a better full ice shelf estimate. The along-flow distribution and initial-pixel basal melt rates are comparable on the outer ice shelf and slow-moving areas of the North and South ice shelves, with both offering good resolution of basal melt rates for longitudinal surface features (e.g., channels and keels).

The spatial distribution of high basal melt rates near the grounding line (Figure S4) is likely a function of modern (post-2006) cavity geometry (Figure S1) and sub-shelf circulation. Mass conserving bed reconstruction for the 1990s configuration revealed a large longitudinal seabed ridge (~4 km wide x 30 km long) near the centerline of the inner cavity (Rignot et al., 2014). The highest basal melt rates of >200–250 m/yr are observed on the north side of this longitudinal seabed ridge, where warm, salty water circulating at depth through the inner cavity first reaches the grounding line (e.g., Dutrieux et al., 2014b).

The enhanced ~30–40 m/yr basal melt rates over the northern portion of the outer ice shelf (red arrow in Figure 9) are located immediately downstream of the transverse seabed ridge (Figure S1). Both the Autosub observations and ocean GCM simulations show increased ocean current velocity and enhanced variability due to cold water intrusion near this location (Dutrieux et al., 2014b), suggesting that this local high in basal melt rates could be related to local circulation patterns and/or upwelling. This location is also one of the expected pathways for warm CDW inflow into the inner cavity (e.g., St-Laurent et al., 2015), and we suggest that as this water flows over the transverse seabed ridge, it could lead to enhanced turbulence, vertical heat transport towards the ice base, and increased basal melting.

5.3 Channel-scale melt distribution

Our results are generally consistent with past work (e.g., Dutrieux et al., 2013) suggesting that higher melt rates are associated with basal channels in the inner cavity, and basal keels over the outer ice shelf (Figure 10). Inner-cavity channels/keels have much higher relief than outer ice shelf channels/keels, so we might expect higher basal melt rates due to faster plume-driven flow along inner-cavity channels. However, our results also show high basal melt rates over deep keels in the inner cavity,

Field Code Changed

Deleted: Figure 7

Deleted: -wide

Deleted: steep

Deleted: -wide

Deleted: "

Deleted: "

Deleted: individual

Deleted: We note that t

Deleted: Figure 8

Deleted: just

Field Code Changed

Deleted: associated

Deleted: increased

Deleted: melt

Deleted: occurs

Deleted: within

Deleted: deep

Deleted: closer to the grounding line

Deleted: on

Deleted: Figure 9

Deleted: -

Deleted: we also observe

825 especially within ~5 km of the grounding line (Figure S5), suggesting that high heat content and local circulation may dominate basal melting at these depths.

Our results demonstrate the potential for high-resolution Lagrangian Dh/Dt measurements of channel-scale features on ice shelves, even with known methodological limitations (see Section 2.10; discussion in Dutrieux et al., 2013; Shean et al., 2017). Keels on the mid to outer PIG ice shelf typically reach water depths up to ~400–450 m, while channels are typically ~300–350 m. These features should intersect the observed thermocline, with temperature gradients of over 1.0°C possible between ~300 and ~450 m depth (Dutrieux et al., 2014b). Our results are consistent with the hypothesis that enhanced melting of outer ice shelf keels is related to their exposure to warmer water at depth (end member #1 in Section 3.5), with reduced plume-driven flow in the channels due to limited ice thickness gradients. The transverse surface ridges and troughs on the south side of the main ice shelf display greater relief than those along the north side of the ice shelf (Figure 3), with correspondingly higher basal melt rates over the deeper keels (Figure 10). Based on these preliminary results, we suggest that analysis of keel melt rates over time could provide new information about the spatiotemporal evolution of the thermocline in the outer cavity.

5.4 Comparison with past basal melt-rate assessments

840 The local basal melt rates observed near the grounding line within the deep inner cavity (>200 m/yr, Figure 9 and S4) are significantly higher than some past estimates of ~100 m/yr from observations (Bindschadler et al., 2011; Dutrieux et al., 2013) and ~70–120 m/yr from ocean circulation modeling (Dutrieux et al., 2014b; Payne et al., 2007; Seroussi et al., 2014). They are more consistent with flux divergence melt rate estimates of ~200–300 m/yr near the mid-1990s grounding line by Payne et al. (2007) and ~200 m/yr near the 2009 grounding line by Dutrieux et al. (2013).

Our full ice shelf mean basal melt rates for the period between 2008 and 2015 (~82–93 Gt/yr) are less than, but within the reported uncertainty of past estimates for the period between 2003 and 2008: 95±/−14 (Depoorter et al., 2013) and 101±/−8 Gt/yr (Rignot et al., 2013). While it is possible that no change occurred between the 2003–2008 period and the 2008–2015 period, the apparent decrease in mean melt rate would be consistent with melt rate estimates from oceanographic observations of ~100 Gt/yr in 2007 to ~73 Gt/yr in 2009 (Dutrieux et al., 2014b). However, this apparent decrease may be at least partially attributable to methodological differences between our study and previous studies (e.g., ice shelf area, flux-gate placement). The previous studies also mixed observations from different time intervals during a highly dynamic period in PIG's recent history, with dh/dt from JCESat data acquired between 2003 and 2008, velocities from an InSAR mosaic with approximate timestamp of 2007–2008 (Rignot et al., 2011), and average SMB for the period from 1979 to 2010. Furthermore, these studies relied on interpolation of sparse JCESat tracks to estimate spatially continuous Eulerian dH/dt for the entire PIG ice shelf (e.g., -5.32±/−0.3 m/yr (Rignot et al., 2013)). The JCESat GLAS laser spot was ~30–70 m in diameter with ~170 m along-track spacing and ~20 km cross-track spacing between repeat tracks over PIG (e.g., Figure 3 of Pritchard et al. (2009)). Limited measurements were available to constrain local slopes sampled by repeat JCESat tracks over the PIG ice shelf, and aliasing of advecting km-scale surface ridges and troughs can lead to significant errors in thinning rates inferred from smoothed JCESat repeat tracks (e.g. Figure 13 of Sergienko (2013)), especially after converting inferred elevation change to freeboard thickness

Deleted: can

Formatted: Font: Italic

Deleted: analyses

Field Code Changed

Deleted: (Section 2.10 and discussion in Dutrieux et al., 2013; Shean et al., 2017)

Deleted: We note that t

Deleted: observations

Deleted: statistical

Deleted: c

Deleted:

Field Code Changed

Deleted: (Bindschadler et al., 2011; Dutrieux et al., 2013; Payne et al., 2007)

Deleted: the

Deleted:

Deleted: estimates, which show high rates of ~200–300 m/yr near the mid-1990s grounding line

Deleted: -

Deleted: -

Deleted: less than

Deleted: of~

Deleted: for the 2003–2008 period

Deleted: While

Deleted: our estimates fall within reported uncertainty, it is possible that this difference could represent a true decrease in shelf-wide melt from 2003–2008 to 2008–2015

Deleted: , which

Deleted: that indicate a decrease from

Deleted: between 2007 and

Deleted: 2003–2008 ICESat-1

Deleted:

Deleted: from

Deleted: -

Deleted: ICESat-1

Deleted: PIG shelf

Deleted: ICESat-1

Deleted: ICESat-1

Deleted: PIG shelf

Deleted: ICESat-1

Field Code Changed

change. While this may not be relevant for relatively flat, smooth ice shelves with high ICESat track density like the Ross and
895 Ronne-Filchner ice shelves (e.g., Moholdt et al., 2014), this issue complicates analysis of the sparse ICESat dh/dt
measurements over the relatively rough PIG ice shelf, and previous uncertainty estimates for full ice shelf basal melt rates
based on ICESat observations are likely too low. Thus, while basal melt rates may have been higher between 2003 and 2008,
we cannot rule out the possibility that no long-term change occurred between the 2003–2008 and 2008–2015 periods.
900 Observations with ~20-km spatial resolution (e.g., ICESat or radar altimetry (e.g., Paolo et al., 2015)) can capture the long-
term temporal evolution of Eulerian elevation change and basal melt for the full PIG ice shelf, but they cannot directly capture
changes associated with dynamic ice-ocean processes that operate on shorter spatial scales. The high-resolution DEM record
and methodology presented here allows for both full ice shelf basal melt rate estimates and analysis of the detailed
spatiotemporal evolution of km-scale features that are coupled to sub-shelf circulation and local basal melting. As the high-
resolution DEM record for Antarctica continues to grow, future analyses for PIG and other Antarctic ice shelves will provide
905 new insight into the underlying processes controlling ice-ocean interaction, with implications for future ice sheet stability.

6 Summary/conclusions

We developed a method to correct and integrate high-resolution DEM observations with satellite/airborne altimetry data and
surface velocity data to estimate Eulerian dh/dt , Lagrangian Dh/Dt , and ice shelf basal melt rates. Mean 2008–2015 basal melt
rates for the full PIG ice shelf were ~82–93 Gt/yr. Local basal melt rates were ~200–250 m/yr near the grounding line, ~10–
910 30 m/yr over the outer main ice shelf, and ~0–10 m/yr over the North and South ice shelves, with notable exception of ~50–
100 m/yr near the grounding line of a fast-flowing tributary on the South ice shelf. The basal melt rates from Lagrangian Dh/Dt
measurements show excellent agreement with, and provide spatial/temporal context for, in situ basal melt rate observations.
Basal melt rates vary substantially across ~km-scale ice shelf thickness variations, with greater melting observed in basal
channels and over deep keels near the grounding line and relatively shallow keels over the outer ice shelf. The methods and
915 general results presented here provide a foundation for further analysis of the detailed spatiotemporal evolution of basal melt
rates and connections with ocean observations for the PIG ice shelf during the 2008–2015 period.

Acknowledgements

D. Shean was supported by NASA NESSF fellowship award NNX12AN36H. I. Joughin was supported by NASA Cryosphere
awards NNX15AD54G and NNX17AG54G and NSF OPP award 1643285. B. Smith was supported by NASA Cryosphere
920 award NNX13AP96G. P. Dutriex was supported by NSF OPP award 1643285 and the UW Applied Physics Laboratory. E.
Berthier was supported by the French Space Agency through the TOSCA program. We acknowledge Claire Porter, Paul Morin,
and others at the Polar Geospatial Center (NSF ANT-1043681) who managed tasking, ordering, and distribution of the L1B
commercial stereo imagery under the NGA NextView license. We thank Oleg Alexandrov, Zack Moratto and Scott McMichael

Deleted: ICESat-1

Field Code Changed

Deleted: -wide

Deleted: ICESat-1

Deleted: from

Deleted: ~

Deleted: -

Deleted: ~

Deleted: to

Deleted: ~

Deleted: We note that o

Deleted: ICESat-1

Deleted: -

Deleted: Lagrangian Dh/Dt

Formatted: Font: Not Italic

Deleted: PIG shelf

for additional development of the Ames Stereo Pipeline with support from the NASA Cryosphere program. We thank Stefan Ligtenberg and Peter Kuipers Munneke for providing RACMO SMB products. Howard Conway and Nick Holschuh offered productive comments on an earlier version of this manuscript. Resources supporting this work were provided by the NASA High-End Computing (HEC) Program through the NASA Advanced Supercomputing (NAS) Division at Ames Research Center. The SPOT-5 DEMs and imagery were provided at no cost by the French Space Agency (CNES) through the SPIRIT International Polar Year project (Korona et al., 2009). We thank two anonymous reviewers for their thoughtful comments and suggestions, which improved this manuscript.

Deleted: continued

Deleted: and FDM

Formatted: Font: Not Bold

Field Code Changed

945 References

Andersen, O. B. and Knudsen, P.: DNSC08 mean sea surface and mean dynamic topography models, J. Geophys. Res., 114(C11), doi:10.1029/2008JC005179, 2009.

Formatted: Bibliography, Widow/Orphan control, Adjust space between Latin and Asian text, Adjust space between Asian text and numbers

Bamber, J. L., Riva, R. E. M., Vermeersen, B. L. A. and LeBrocq, A. M.: Reassessment of the Potential Sea-Level Rise from a Collapse of the West Antarctic Ice Sheet, Science, 324(5929), 901–903, doi:10.1126/science.1169335, 2009.

Field Code Changed

Formatted: Font: 10 pt

950 Bamber, J. L., Westaway, R. M., Marzeion, B. and Wouters, B.: The land ice contribution to sea level during the satellite era, Environ. Res. Lett., 13(6), 063008, doi:10.1088/1748-9326/aac2f0, 2018.

Formatted: Font: 10 pt

Formatted: Font: 10 pt

Barletta, V. R., Bevis, M., Smith, B. E., Wilson, T., Brown, A., Bordoni, A., Willis, M., Khan, S. A., Rovira-Navarro, M., Dalziel, I., Smalley, R., Kendrick, E., Konfal, S., Caccamise, D. J., Aster, R. C., Nyblade, A. and Wiens, D. A.: Observed rapid bedrock uplift in Amundsen Sea Embayment promotes ice-sheet stability, Science, 360(6395), 1335–1339, doi:10.1126/science.aao1447, 2018.

Formatted: Font: 10 pt

955 Berger, S., Drews, R., Helm, V., Sun, S. and Pattyn, F.: Detecting high spatial variability of ice shelf basal mass balance, Roi Baudouin Ice Shelf, Antarctica, The Cryosphere, 11(6), 2675–2690, doi:10.5194/tc-11-2675-2017, 2017.

Formatted: Font: 10 pt

Beyer, R., Alexandrov, O. and ScottMcMichael: NeoGeographyToolkit/StereoPipeline: ASP 2.6.2, Zenodo., 2019.

Formatted: Font: 10 pt

960 Beyer, R. A., Alexandrov, O. and McMichael, S.: The Ames Stereo Pipeline: NASA's Open Source Software for Deriving and Processing Terrain Data, Earth Space Sci., 0(0), doi:10.1029/2018EA000409, 2018.

Formatted: Font: 10 pt

Bindschadler, R., Vaughan, D. G. and Vornberger, P.: Variability of basal melt beneath the Pine Island Glacier ice shelf, West Antarctica, J. Glaciol., 57(204), 581–595, 2011.

Formatted: Font: 10 pt

Bindschadler, R. A.: History of lower Pine Island Glacier, West Antarctica, from Landsat imagery, J. Glaciol., 48(163), 536–544, 2002.

Formatted: Font: 10 pt

965 Blair, J. B., Rabine, D. L. and Hofton, M. A.: The Laser Vegetation Imaging Sensor: a medium-altitude, digitisation-only, airborne laser altimeter for mapping vegetation and topography, ISPRS J. Photogramm. Remote Sens., 54(2), 115–122, 1999.

Formatted: Font: 10 pt

970 Bouillon, A., Bernard, M., Gigord, P., Orsoni, A., Rudowski, V. and Baudoin, A.: SPOT 5 HRS geometric performances: Using block adjustment as a key issue to improve quality of DEM generation, ISPRS J. Photogramm. Remote Sens., 60(3), 134–146, doi:10.1016/j.isprsjprs.2006.03.002, 2006.

Formatted: Font: 10 pt

- 975 Christianson, K., Bushuk, M., Dutrieux, P., Parizek, B. R., Joughin, I. R., Alley, R. B., Shean, D. E., Abrahamsen, E. P., Anandakrishnan, S., Heywood, K. J., Kim, T.-W., Lee, S. H., Nicholls, K., Stanton, T., Truffer, M., Webber, B. G. M., Jenkins, A., Jacobs, S., Bindschadler, R. and Holland, D. M.: Sensitivity of Pine Island Glacier to observed ocean forcing: PIG response to ocean forcing, *Geophys. Res. Lett.*, 43(20), 10.817-10.825, doi:10.1002/2016GL070500, 2016. Formatted: Font: 10 pt
- Church, J. A., Cazenave, A., Gregory, J. M., Jevrejeva, S., Levermann, A., Merrifield, M. A., Milne, G. A., Nerem, R. S., Nunn, P. D., Payne, A. J., Pfeffer, W. T., Stammer, D. and Unnikrishnan, A. S.: Sea Level Change. [online] Available from: http://www.ipcc.ch/pdf/assessment-report/ar5/wg1/WG1AR5_Chapter13_FINAL.pdf (Accessed 6 January 2015), 2013. Formatted: Font: 10 pt
- 980 Csatho, B. M., Schenk, A. F., van der Veen, C. J., Babonis, G., Duncan, K., Rezvanbebahani, S., van den Broeke, M. R., Simonsen, S. B., Nagarajan, S. and van Angelen, J. H.: Laser altimetry reveals complex pattern of Greenland Ice Sheet dynamics, *Proc. Natl. Acad. Sci.*, 201411680, doi:10.1073/pnas.1411680112, 2014. Formatted: Font: 10 pt
- De Rydt, J., Holland, P. R., Dutrieux, P. and Jenkins, A.: Geometric and oceanographic controls on melting beneath Pine Island Glacier, *J. Geophys. Res. Oceans*, 119(4), 2420–2438, doi:10.1002/2013JC009513, 2014. Formatted: Font: 10 pt
- 985 Dee, D. P., Uppala, S. M., Simmons, A. J., Berrisford, P., Poli, P., Kobayashi, S., Andrae, U., Balmaseda, M. A., Balsamo, G., Bauer, P., Bechtold, P., Beljaars, A. C. M., van de Berg, L., Bidlot, J., Bormann, N., Delsol, C., Dragani, R., Fuentes, M., Geer, A. J., Haimberger, L., Healy, S. B., Hersbach, H., Hólm, E. V., Isaksen, L., Kállberg, P., Köhler, M., Matricardi, M., McNally, A. P., Monge-Sanz, B. M., Morcrette, J.-J., Park, B.-K., Peubey, C., de Rosnay, P., Tavolato, C., Thépaut, J.-N. and Vitart, F.: The ERA-Interim reanalysis: configuration and performance of the data assimilation system, *Q. J. R. Meteorol. Soc.*, 137(656), 553–597, doi:10.1002/qj.828, 2011. Formatted: Font: 10 pt
- 990 Depoorter, M. A., Bamber, J. L., Griggs, J. A., Lenaerts, J. T. M., Ligtenberg, S. R. M., van den Broeke, M. R. and Moholdt, G.: Calving fluxes and basal melt rates of Antarctic ice shelves, *Nature*, 502, 89–92, doi:10.1038/nature12567, 2013. Formatted: Font: 10 pt
- Dutrieux, P., Vaughan, D. G., Corr, H. F. J., Jenkins, A., Holland, P. R., Joughin, I. and Fleming, A. H.: Pine Island glacier ice shelf melt distributed at kilometre scales, *The Cryosphere*, 7(5), 1543–1555, doi:10.5194/tc-7-1543-2013, 2013. Formatted: Font: 10 pt
- 995 Dutrieux, P., Stewart, C., Jenkins, A., Nicholls, K. W., Corr, H. F. J., Rignot, E. and Steffen, K.: Basal terraces on melting ice shelves, *Geophys. Res. Lett.*, n/a-n/a, doi:10.1002/2014GL060618, 2014a. Formatted: Font: 10 pt
- Dutrieux, P., De Rydt, J., Jenkins, A., Holland, P. R., Ha, H. K., Lee, S. H., Steig, E. J., Ding, Q., Abrahamsen, E. P. and Schroder, M.: Strong Sensitivity of Pine Island Ice-Shelf Melting to Climatic Variability, *Science*, 343(6167), 174–178, doi:10.1126/science.1244341, 2014b. Formatted: Font: 10 pt
- 000 Ettema, J., van den Broeke, M. R., van Meijgaard, E., van de Berg, W. J., Bamber, J. L., Box, J. E. and Bales, R. C.: Higher surface mass balance of the Greenland ice sheet revealed by high-resolution climate modeling, *Geophys. Res. Lett.*, 36(12), L12501, doi:10.1029/2009GL038110, 2009. Formatted: Font: 10 pt
- Flament, T. and Rémy, F.: Dynamic thinning of Antarctic glaciers from along-track repeat radar altimetry, *J. Glaciol.*, 58(211), 830–840, doi:10.3189/2012JoGI1J1118, 2012. Formatted: Font: 10 pt
- 005 Fretwell, P., Pritchard, H. D., Vaughan, D. G., Bamber, J. L., Barrand, N. E., Bell, R., Bianchi, C., Bingham, R. G., Blankenship, D. D., Casassa, G., Catania, G., Callens, D., Conway, H., Cook, A. J., Corr, H. F. J., Damaske, D., Damm, V., Ferraccioli, F., Forsberg, R., Fujita, S., Gim, Y., Gogineni, P., Griggs, J. A., Hindmarsh, R. C. A., Holmlund, P., Holt, J. W., Jacobel, R. W., Jenkins, A., Jokat, W., Jordan, T., King, E. C., Kohler, J., Krabill, W., Riger-Kusk, M., Langley, K. A., Leitchenkov, G., Leuschen, C., Luyendyk, B. P., Matsuoka, K., Mougouinot, J., Nitsche, F. O., Nogi, Y., Nost, O. A., Popov, S. V., Rignot, E., Rippon, D. M., Rivera, A., Roberts, J., Ross, N., Siegert, M. J., Smith, A. M., Steinhage, D., Studinger, M., Formatted: Font: 10 pt

- Sun, B., Tinto, B. K., Welch, B. C., Wilson, D., Young, D. A., Xiangbin, C. and Zirizzotti, A.: Bedmap2: improved ice bed, surface and thickness datasets for Antarctica, *The Cryosphere*, 7(1), 375–393, doi:10.5194/tc-7-375-2013, 2013.
- 015 Groh, A., Ewert, H., Scheinert, M., Fritsche, M., Rülke, A., Richter, A., Rosenau, R. and Dietrich, R.: An investigation of Glacial Isostatic Adjustment over the Amundsen Sea sector, West Antarctica, *Glob. Planet. Change*, 98–99, 45–53, doi:10.1016/j.gloplacha.2012.08.001, 2012.
- Gunter, B. C., Didova, O., Riva, R. E. M., Ligtenberg, S. R. M., Lenaerts, J. T. M., King, M. A., van den Broeke, M. R. and Urban, T.: Empirical estimation of present-day Antarctic glacial isostatic adjustment and ice mass change, *The Cryosphere*, 8(2), 743–760, doi:10.5194/tc-8-743-2014, 2014.
- 020 Hofton, M. A., Blair, J. B., Luthcke, S. B. and Rabine, D. L.: Assessing the performance of 20–25 m footprint waveform lidar data collected in ICESat data corridors in Greenland, *Geophys. Res. Lett.*, 35(24), doi:10.1029/2008GL035774, 2008.
- Jacobs, S., Jenkins, A., Hellmer, H., Giulivi, C., Nitsche, F., Huber, B. and Guerrero, R.: The Amundsen Sea and the Antarctic Ice Sheet, *Oceanography*, 25(3), 154–163, doi:10.5670/oceanog.2012.90, 2012.
- Jacobs, S. S., Hellmer, H. H. and Jenkins, A.: Antarctic ice sheet melting in the Southeast Pacific, *Geophys. Res. Lett.*, 23(9), 957–960, 1996.
- 025 Jacobs, S. S., Jenkins, A., Giulivi, C. F. and Dutriex, P.: Stronger ocean circulation and increased melting under Pine Island Glacier ice shelf, *Nat. Geosci.*, 4(8), 519–523, doi:10.1038/ngeo1188, 2011.
- Jakobsson, M., Anderson, J. B., Nitsche, F. O., Gyllencreutz, R., Kirshner, A. E., Kirchner, N., O'Regan, M., Mohammad, R. and Eriksson, B.: Ice sheet retreat dynamics inferred from glacial morphology of the central Pine Island Bay Trough, West Antarctica, *Quat. Sci. Rev.*, 38, 1–10, doi:10.1016/j.quascirev.2011.12.017, 2012.
- 030 Jenkins, A., Vaughan, D. G., Jacobs, S. S., Hellmer, H. H. and Keys, J. R.: Glaciological and oceanographic evidence of high melt rates beneath Pine Island Glacier, West Antarctica, *J. Glaciol.*, 43(143), 114–121, 1997.
- Jenkins, A., Corr, H. F., Nicholls, K. W., Stewart, C. L. and Doake, C. S.: Interactions between ice and ocean observed with phase-sensitive radar near an Antarctic ice-shelf grounding line, *J. Glaciol.*, 52(178), 325–346, 2006.
- 035 Jenkins, A., Dutriex, P., Jacobs, S. S., McPhail, S. D., Perrett, J. R., Webb, A. T. and White, D.: Observations beneath Pine Island Glacier in West Antarctica and implications for its retreat, *Nat. Geosci.*, 3(7), 468–472, doi:10.1038/ngeo890, 2010.
- Jenkins, A., Shoosmith, D., Dutriex, P., Jacobs, S., Kim, T. W., Lee, S. H., Ha, H. K. and Stammerjohn, S.: West Antarctic Ice Sheet retreat in the Amundsen Sea driven by decadal oceanic variability, *Nat. Geosci.*, doi:10.1038/s41561-018-0207-4, 2018.
- 040 Joughin, I.: Ice-sheet velocity mapping: a combined interferometric and speckle-tracking approach, *Ann. Glaciol.*, 34(1), 195–201, 2002.
- Joughin, I. and Alley, R. B.: Stability of the West Antarctic ice sheet in a warming world, *Nat. Geosci.*, 4, 506–513, doi:10.1038/ngeo1194, 2011.
- Joughin, I. and Padman, L.: Melting and freezing beneath Filchner-Ronne Ice Shelf, Antarctica, *Geophys Res Lett*, 30(9), 1477, doi:10.1029/2003GL016941, 2003.

045 Joughin, I., Rignot, E., Rosanova, C. E., Lucchitta, B. K. and Bohlander, J.: Timing of Recent Accelerations of Pine Island Glacier, Antarctica, Geophys. Res. Lett., 30(13), doi:10.1029/2003GL017609, 2003.

Formatted: Font: 10 pt

Joughin, I., Smith, B. E. and Holland, D. M.: Sensitivity of 21st century sea level to ocean-induced thinning of Pine Island Glacier, Antarctica, Geophys. Res. Lett., 37(20), L20502, doi:10.1029/2010GL044819, 2010.

Formatted: Font: 10 pt

050 Joughin, I., Shean, D. E., Smith, B. E. and Dutrieux, P.: Grounding line variability and subglacial lake drainage on Pine Island Glacier, Antarctica, Geophys. Res. Lett., 43(17), 9093–9102, doi:10.1002/2016GL070259, 2016.

Formatted: Font: 10 pt

Kirshner, A. E., Anderson, J. B., Jakobsson, M., O'Regan, M., Majewski, W. and Nitsche, F. O.: Post-LGM deglaciation in Pine Island Bay, West Antarctica, Quat. Sci. Rev., 38, 11–26, doi:10.1016/j.quascirev.2012.01.017, 2012.

Formatted: Font: 10 pt

Kobs, S., Holland, D. M., Zagorodnov, V., Stern, A. and Tyler, S. W.: Novel monitoring of Antarctic ice shelf basal melting using a fiber-optic distributed temperature sensing mooring: Novel monitoring of Antarctic ice shelf, Geophys. Res. Lett., n/a-n/a, doi:10.1002/2014GL061155, 2014.

Formatted: Font: 10 pt

055 Konrad, H., Shepherd, A., Gilbert, L., Hogg, A. E., McMillan, M., Muir, A. and Slater, T.: Net retreat of Antarctic glacier grounding lines, Nat. Geosci., 11(4), 258–262, doi:10.1038/s41561-018-0082-z, 2018.

Formatted: Font: 10 pt

Korona, J., Berthier, E., Bernard, M., Rémy, F. and Thouvenot, E.: SPIRIT. SPOT 5 stereoscopic survey of polar ice: Reference images and topographies during the fourth international polar year (2007–2009), ISPRS J. Photogramm. Remote Sens., 64(2), 204–212, 2009.

Formatted: Font: 10 pt

060 Krabill, W. B., Abdalati, W., Frederick, E. B., Manizade, S. S., Martin, C. F., Sonntag, J. G., Swift, R. N., Thomas, R. H. and Yungel, J. G.: Aircraft laser altimetry measurement of elevation changes of the Greenland ice sheet: Technique and accuracy assessment, J. Geodyn., 34(3), 357–376, 2002.

Formatted: Font: 10 pt

Langley, K., Kohler, J., Sinisalo, A., Øyan, M. J., Hamran, S. E., Hattermann, T., Matsuoka, K., Nøst, O. A. and Isaksson, E.: Low melt rates with seasonal variability at the base of Fimbul Ice Shelf, East Antarctica, revealed by in situ interferometric radar measurements, Geophys. Res. Lett., n/a-n/a, doi:10.1002/2014GL061782, 2014.

Formatted: Font: 10 pt

Lenaerts, J. T. M., van den Broeke, M. R., van de Berg, W. J., van Meijgaard, E. and Kuipers Munneke, P.: A new, high-resolution surface mass balance map of Antarctica (1979–2010) based on regional atmospheric climate modeling, Geophys. Res. Lett., 39(4), L04501, doi:10.1029/2011GL050713, 2012.

Formatted: Font: 10 pt

070 Marsh, O. J., Fricker, H. A., Siegfried, M. R., Christianson, K., Nicholls, K. W., Corr, H. F. J. and Catania, G.: High basal melting forming a channel at the grounding line of Ross Ice Shelf, Antarctica, Geophys. Res. Lett., n/a-n/a, doi:10.1002/2015GL066612, 2015.

Formatted: Font: 10 pt

Martin, C. F., Krabill, W. B., Manizade, S. S., Russell, R. L., Sonntag, J. G., Swift, R. N. and Yungel, J. K.: Airborne topographic mapper calibration procedures and accuracy assessment, Technical Memorandum, National Aeronautics and Space Administration, Goddard Space Flight Center. [online] Available from: <http://ntrs.nasa.gov/archive/nasa/casi.ntrs.nasa.gov/20120008479.pdf> (Accessed 22 January 2016), 2012.

Formatted: Font: 10 pt

075 Medley, B., Joughin, I., Smith, B. E., Das, S. B., Steig, E. J., Conway, H., Gogineni, S., Lewis, C., Criscitiello, A. S., McConnell, J. R., van den Broeke, M. R., Lenaerts, J. T. M., Bromwich, D. H., Nicolas, J. P. and Leuschen, C.: Constraining the recent mass balance of Pine Island and Thwaites glaciers, West Antarctica, with airborne observations of snow accumulation, The Cryosphere, 8(4), 1375–1392, doi:10.5194/tc-8-1375-2014, 2014.

Formatted: Font: 10 pt

080

- 085 [Milillo, P., Rignot, E., Mouginot, J., Scheuchl, B., Morlighem, M., Li, X. and Salzer, J. T.: On the Short-term Grounding Zone Dynamics of Pine Island Glacier, West Antarctica, Observed With COSMO-SkyMed Interferometric Data: PIG Grounding Line Dynamics, *Geophys. Res. Lett.*, doi:10.1002/2017GL074320, 2017.](#) Formatted: Font: 10 pt
- [Moholdt, G., Padman, L. and Fricker, H. A.: Basal mass budget of Ross and Filchner-Ronne ice shelves, Antarctica, derived from Lagrangian analysis of ICESat altimetry: Ice shelf basal melting from altimetry, *J. Geophys. Res. Earth Surf.*, 119\(11\), 2361–2380, doi:10.1002/2014JF003171, 2014.](#) Formatted: Font: 10 pt
- [Morlighem, M., Rignot, E., Seroussi, H., Larour, E., Dhia, H. B. and Aubry, D.: A mass conservation approach for mapping glacier ice thickness, *Geophys. Res. Lett.*, 38\(19\), L19503, 2011.](#) Formatted: Font: 10 pt
- 090 [Mouginot, J., Rignot, E. and Scheuchl, B.: Sustained increase in ice discharge from the Amundsen Sea Embayment, West Antarctica, from 1973 to 2013, *Geophys. Res. Lett.*, 41\(5\), 1576–1584, doi:10.1002/2013GL059069, 2014.](#) Formatted: Font: 10 pt
- [Mueller, R. D., Padman, L., Dinniman, M. S., Erofeeva, S. Y., Fricker, H. A. and King, M. A.: Impact of tide-topography interactions on basal melting of Larsen C Ice Shelf, Antarctica: LARSEN C TIDES AND BASAL MELT, *J. Geophys. Res. Oceans*, 117\(C5\), n/a-n/a, doi:10.1029/2011JC007263, 2012.](#) Formatted: Font: 10 pt
- 095 [Muto, A., Peters, L. E., Gohl, K., Sasgen, I., Alley, R. B., Anandakrishnan, S. and Riverman, K. L.: Subglacial bathymetry and sediment distribution beneath Pine Island Glacier ice shelf modeled using aerogravity and in situ geophysical data: New results, *Earth Planet. Sci. Lett.*, 433, 63–75, doi:10.1016/j.epsl.2015.10.037, 2016.](#) Formatted: Font: 10 pt
- [Padman, L., Fricker, H. A., Coleman, R., Howard, S. and Erofeeva, L.: A new tide model for the Antarctic ice shelves and seas, *Ann. Glaciol.*, 34\(1\), 247–254, 2002.](#) Formatted: Font: 10 pt
- 100 [Padman, L., King, M., Goring, D., Corr, H. and Coleman, R.: Ice-shelf elevation changes due to atmospheric pressure variations, *J. Glaciol.*, 49\(167\), 521–526, doi:10.3189/172756503781830386, 2003.](#) Formatted: Font: 10 pt
- [Paolo, F. S., Fricker, H. A. and Padman, L.: Volume loss from Antarctic ice shelves is accelerating, *Science*, 348\(6232\), 327–331, doi:10.1126/science.aaa0940, 2015.](#) Formatted: Font: 10 pt
- [Park, J. W., Gourmelen, N., Shepherd, A., Kim, S. W., Vaughan, D. G. and Wingham, D. J.: Sustained retreat of the Pine Island Glacier, *Geophys. Res. Lett.*, n/a-n/a, doi:10.1002/grl.50379, 2013.](#) Formatted: Font: 10 pt
- 105 [Pavlis, N. K., Holmes, S. A., Kenyon, S. C. and Factor, J. K.: The development and evaluation of the Earth Gravitational Model 2008 \(EGM2008\), *J. Geophys. Res.*, 117\(B4\), B04406, doi:10.1029/2011JB008916, 2012.](#) Formatted: Font: 10 pt
- [Payne, A. J., Holland, P. R., Shepherd, A. P., Rutt, I. C., Jenkins, A. and Joughin, I.: Numerical modeling of ocean-ice interactions under Pine Island Bay's ice shelf, *J. Geophys. Res.*, 112\(C10\), doi:10.1029/2006JC003733, 2007.](#) Formatted: Font: 10 pt
- 110 [Pritchard, H. D., Arthern, R. J., Vaughan, D. G. and Edwards, L. A.: Extensive dynamic thinning on the margins of the Greenland and Antarctic ice sheets, *Nature*, 461\(7266\), 971–975, doi:10.1038/nature08471, 2009.](#) Formatted: Font: 10 pt
- [Pritchard, H. D., Ligtenberg, S. R. M., Fricker, H. A., Vaughan, D. G., van den Broeke, M. R. and Padman, L.: Antarctic ice-sheet loss driven by basal melting of ice shelves, *Nature*, 484\(7395\), 502–505, doi:10.1038/nature10968, 2012.](#) Formatted: Font: 10 pt
- [Rietbroek, R., Brunnabend, S.-E., Kusche, J., Schröter, J. and Dahle, C.: Revisiting the contemporary sea-level budget on global and regional scales, *Proc. Natl. Acad. Sci.*, 113\(6\), 1504–1509, 2016.](#) Formatted: Font: 10 pt

- 115 [Rignot, E.: Changes in West Antarctic ice stream dynamics observed with ALOS PALSAR data, *Geophys Res Lett*, 35\(12\), L12505, doi:10.1029/2008GL033365, 2008.](#) Formatted: Font: 10 pt
- [Rignot, E. and Jacobs, S.: Rapid Bottom Melting Widespread near Antarctic Ice Sheet Grounding Lines, *Science*, 296\(5575\), 2020–2023, doi:10.1126/science.1070942, 2002.](#) Formatted: Font: 10 pt
- 120 [Rignot, E., Mouginot, J. and Scheuchl, B.: Ice Flow of the Antarctic Ice Sheet, *Science*, 333\(6048\), 1427–1430, doi:10.1126/science.1208336, 2011.](#) Formatted: Font: 10 pt
- [Rignot, E., Jacobs, S., Mouginot, J. and Scheuchl, B.: Ice-Shelf Melting Around Antarctica, *Science*, 341\(6143\), 266–270, doi:10.1126/science.1235798, 2013.](#) Formatted: Font: 10 pt
- [Rignot, E., Mouginot, J., Morlighem, M., Seroussi, H. and Scheuchl, B.: Widespread, rapid grounding line retreat of Pine Island, Thwaites, Smith, and Kohler glaciers, West Antarctica, from 1992 to 2011, *Geophys. Res. Lett.*, 41\(10\), 3502–3509, doi:10.1002/2014GL060140, 2014.](#) Formatted: Font: 10 pt
- 125 [Rignot, E. J.: Fast Recession of a West Antarctic Glacier, *Science*, 281\(5376\), 549–551, doi:10.1126/science.281.5376.549, 1998.](#) Formatted: Font: 10 pt
- [Schenk, T. and Csatho, B.: A New Methodology for Detecting Ice Sheet Surface Elevation Changes From Laser Altimetry Data, *IEEE Trans. Geosci. Remote Sens.*, 50\(9\), 3302–3316, doi:10.1109/TGRS.2011.2182357, 2012.](#) Formatted: Font: 10 pt
- 130 [Schodlok, M. P., Menemenlis, D., Rignot, E. and Studinger, M.: Sensitivity of the ice-shelf/ocean system to the sub-ice-shelf cavity shape measured by NASA IceBridge in Pine Island Glacier, West Antarctica, *Ann. Glaciol.*, 53\(60\), 156–162, doi:10.3189/2012AoG60A073, 2012.](#) Formatted: Font: 10 pt
- [Schoof, C.: Ice sheet grounding line dynamics: Steady states, stability, and hysteresis, *J Geophys Res*, 112\(10.1029\), 2007.](#) Formatted: Font: 10 pt
- 135 [Schutz, B. E., Zwally, H. J., Shuman, C. A., Hancock, D. and DiMarzio, J. P.: Overview of the ICESat Mission, *Geophys. Res. Lett.*, 32\(21\), doi:10.1029/2005GL024009, 2005.](#) Formatted: Font: 10 pt
- [Scott, J. B., Smith, A. M., Bingham, R. G. and Vaughan, D. G.: Crevasses triggered on Pine Island Glacier, West Antarctica, by drilling through an exceptional melt layer, *Ann. Glaciol.*, 51\(55\), 65–70, 2010.](#) Formatted: Font: 10 pt
- [Sergienko, O. V.: Basal channels on ice shelves, *J. Geophys. Res. Earth Surf.*, 118\(3\), 1342–1355, doi:10.1002/jgrf.20105, 2013.](#) Formatted: Font: 10 pt
- 140 [Seroussi, H., Morlighem, M., Rignot, E., Mouginot, J., Larour, E., Schodlok, M. and Khazendar, A.: Sensitivity of the dynamics of Pine Island Glacier, West Antarctica, to climate forcing for the next 50 years, *The Cryosphere*, 8\(5\), 1699–1710, doi:10.5194/tc-8-1699-2014, 2014.](#) Formatted: Font: 10 pt
- [Shean, D.: Quantifying ice-shelf basal melt and ice-stream dynamics using high-resolution DEM and GPS time series, Ph.D. Thesis, University of Washington, Seattle, WA, 14 July. \[online\] Available from: https://digital.lib.washington.edu/443/researchworks/handle/1773/36365 \(Accessed 21 November 2016\), 2016.](#) Formatted: Font: 10 pt
- 145 [Shean, D. E., Alexandrov, O., Moratto, Z. M., Smith, B. E., Joughin, I. R., Porter, C. and Morin, P.: An automated, open-source pipeline for mass production of digital elevation models \(DEMs\) from very-high-resolution commercial stereo satellite imagery, *ISPRS J. Photogramm. Remote Sens.*, 116, 101–117, doi:10.1016/j.isprsjprs.2016.03.012, 2016.](#) Formatted: Font: 10 pt

150 Shean, D. E., Christianson, K., Larson, K. M., Ligtenberg, S. R. M., Joughin, I. R., Smith, B. E., Stevens, C. M., Bushuk, M. and Holland, D. M.: GPS-derived estimates of surface mass balance and ocean-induced basal melt for Pine Island Glacier ice shelf, Antarctica, The Cryosphere, 11(6), 2655–2674, doi:10.5194/tc-11-2655-2017, 2017.

Formatted: Font: 10 pt

Shepherd, A., Wingham, D. and Rignot, E.: Warm ocean is eroding West Antarctic ice sheet, Geophys Res Lett, 31(23), L23404, 2004.

Formatted: Font: 10 pt

155 Shepherd, A., Wingham, D., Wallis, D., Giles, K., Laxon, S. and Sundal, A. V.: Recent loss of floating ice and the consequent sea level contribution, Geophys. Res. Lett., 37(13), n/a-n/a, doi:10.1029/2010GL042496, 2010.

Formatted: Font: 10 pt

Smith, J. A., Andersen, T. J., Shortt, M., Gaffney, A. M., Truffer, M., Stanton, T. P., Bindschadler, R., Dutrieux, P., Jenkins, A., Hillenbrand, C.-D., Ehrmann, W., Corr, H. F. J., Farley, N., Crowhurst, S. and Vaughan, D. G.: Sub-ice-shelf sediments record history of twentieth-century retreat of Pine Island Glacier, Nature, 541(7635), 77–80, doi:10.1038/nature20136, 2016.

Formatted: Font: 10 pt

160 Stanton, T. P., Shaw, W. J., Truffer, M., Corr, H. F. J., Peters, L. E., Riverman, K. L., Bindschadler, R., Holland, D. M. and Anandakrishnan, S.: Channelized Ice Melting in the Ocean Boundary Layer Beneath Pine Island Glacier, Antarctica, Science, 341(6151), 1236–1239, doi:10.1126/science.1239373, 2013.

Formatted: Font: 10 pt

St-Laurent, P., Klinck, J. M. and Dinniman, M. S.: Impact of local winter cooling on the melt of Pine Island Glacier, Antarctica, J. Geophys. Res. Oceans, n/a-n/a, doi:10.1002/2015JC010709, 2015.

Formatted: Font: 10 pt

165 Sutterley, T. C., Velicogna, I., Rignot, E., Mougnot, J., Flament, T., van den Broeke, M. R., van Wessem, J. M. and Reijmer, C. H.: Mass loss of the Amundsen Sea Embayment of West Antarctica from four independent techniques, Geophys. Res. Lett., 41(23), 8421–8428, doi:10.1002/2014GL061940, 2014.

Formatted: Font: 10 pt

The IMBIE team: Mass balance of the Antarctic Ice Sheet from 1992 to 2017, Nature, 558(7709), 219–222, doi:10.1038/s41586-018-0179-y, 2018.

Formatted: Font: 10 pt

170 Thoma, M., Jenkins, A., Holland, D. and Jacobs, S.: Modelling circumpolar deep water intrusions on the Amundsen Sea continental shelf, Antarctica, Geophys. Res. Lett., 35(18), 2008.

Formatted: Font: 10 pt

Thomas, R., Rignot, E., Kanagaratnam, P., Krabill, W. and Casassa, G.: Force-perturbation analysis of Pine Island Glacier, Antarctica, suggests cause for recent acceleration, Ann. Glaciol., 39(1), 133–138, 2004.

Formatted: Font: 10 pt

175 Van Meijgaard, E., Van Ulf, L. H., Van de Berg, W. J., Bosveld, F. C., Van den Hurk, B., Lenderink, G. and Siebesma, A. P.: The KNMI regional atmospheric climate model RACMO version 2.1, Koninklijk Nederlands Meteorologisch Instituut, [online] Available from: http://www.weeralarm.nl/publications/fulltexts/tr302_racmo2v1.pdf (Accessed 31 May 2013), 2008.

Formatted: Font: 10 pt

180 Van Wessem, J. M., Reijmer, C. H., Morlighem, M., Mougnot, J., Rignot, E., Medley, B., Joughin, I., Wouters, B., Depoorter, M. A., Bamber, J. L., Lenaerts, J. T. M., De Van Berg, W. J., Van Den Broeke, M. R. and Van Meijgaard, E.: Improved representation of East Antarctic surface mass balance in a regional atmospheric climate model, J. Glaciol., 60(222), 761–770, doi:10.3189/2014JG14J051, 2014.

Formatted: Font: 10 pt

Vaughan, D. G., Corr, H. F. J., Bindschadler, R. A., Dutrieux, P., Gudmundsson, G. H., Jenkins, A., Newman, T., Vornberger, P. and Wingham, D. J.: Subglacial melt channels and fracture in the floating part of Pine Island Glacier, Antarctica, J. Geophys. Res., 117(F3), F03012, doi:10.1029/2012JF002360, 2012.

Formatted: Font: 10 pt

185 Velicogna, I., Sutterley, T. C. and van den Broeke, M. R.: Regional acceleration in ice mass loss from Greenland and Antarctica using GRACE time-variable gravity data, Geophys. Res. Lett., n/a-n/a, doi:10.1002/2014GL061052, 2014.

Formatted: Font: 10 pt

WCRP Global Sea Level Budget Group: Global sea-level budget 1993–present, Earth Syst. Sci. Data, 10(3), 1551–1590, doi:https://doi.org/10.5194/essd-10-1551-2018, 2018.

Webber, B. G. M., Heywood, K. J., Stevens, D. P., Dutrieux, P., Abrahamsen, E. P., Jenkins, A., Jacobs, S. S., Ha, H. K., Lee, S. H. and Kim, T. W.: Mechanisms driving variability in the ocean forcing of Pine Island Glacier, Nat. Commun., 8, 14507, doi:10.1038/ncomms14507, 2017.

Weertman, J.: Stability of the junction of an ice sheet and an ice shelf, J. Glaciol., 13, 3–11, 1974.

Wilson, N., Straneo, F. and Heimbach, P.: Satellite-derived submarine melt rates and mass balance (2011–2015) for Greenland's largest remaining ice tongues, The Cryosphere, 11(6), 2773–2782, doi:10.5194/tc-11-2773-2017, 2017.

Wingham, D. J., Wallis, D. W. and Shepherd, A.: Spatial and temporal evolution of Pine Island Glacier thinning, 1995–2006, Geophys. Res. Lett., 36(17), L17501, doi:10.1029/2009GL039126, 2009.

Zwally, H. J., Schutz, B., Abdalati, W., Abshire, J., Bentley, C., Brenner, A., Bufton, J., Dezio, J., Hancock, D. and Harding, D.: ICESat's laser measurements of polar ice, atmosphere, ocean, and land, J. Geodyn., 34(3), 405–445, 2002.

Formatted: Font: 10 pt

Formatted: Font: 10 pt

Formatted: Font: 10 pt

Formatted: Font: 10 pt

Formatted: Font: 10 pt

Formatted: Font: 10 pt

Deleted: Andersen, O. B. and Knudsen, P.: DNSCO8 mean sea surface and mean dynamic topography models, J. Geophys. Res., 114(C11), doi:10.1029/2008JC005179, 2009.¶

Bamber, J. L., Riva, R. E. M., Vermeersen, B. L. A. and LeBrocq, A. M.: Reassessment of the Potential Sea-Level Rise from a Collapse of the West Antarctic Ice Sheet, Science, 324(5929), 901–903, doi:10.1126/science.1169335, 2009.¶

Bamber, J. L., Westaway, R. M., Marzeion, B. and Wouters, B.: The land ice contribution to sea level during the satellite era, Environ. Res. Lett., 13(6), 063008, doi:10.1088/1748-9326/aac2f0, 2018.¶

Barletta, V. R., Bevis, M., Smith, B. E., Wilson, T., Brown, A., Bordoni, A., Willis, M., Khan, S. A., Rovira-Navarro, M., Dalziel, I., Smalley, R., Kendrick, E., Konfal, S., Caccamise, D. J., Aster, R. C., Nyblade, A. and Wiens, D. A.: Observed rapid bedrock uplift in Amundsen Sea Embayment promotes ice-sheet stability, Science, 360(6395), 1335–1339, doi:10.1126/science.aao1447, 2018.¶

Berger, S., Drews, R., Helm, V., Sun, S. and Pattyn, F.: Detecting high spatial variability of ice shelf basal mass balance, Roi Baudouin Ice Shelf, Antarctica, The Cryosphere, 11(6), 2675–2690, doi:10.5194/tc-11-2675-2017, 2017.¶

Beyer, R. A., Alexandrov, O. and McMichael, S.: The Ames Stereo Pipeline: NASA's Open Source Software for Deriving and Processing Terrain Data, Earth Space Sci., 0(0), doi:10.1029/2018EA000409, 2018.¶

Bindschadler, R., Vaughan, D. G. and Vornberger, P.: Variability of basal melt beneath the Pine Island Glacier ice shelf, West Antarctica, J. Glaciol., 57(204), 581–595, 2011.¶

Bindschadler, R. A.: History of lower Pine Island Glacier, West Antarctica, from Landsat imagery, J. Glaciol., 48(163), 536–544, 2002.¶

Blair, J. B., Rabine, D. L. and Hofton, M. A.: The Laser Vegetation Imaging Sensor: a medium-altitude, digitisation-only, airborne laser altimeter for mapping vegetation and topography, ISPRS J. Photogramm. Remote Sens., 54(2), 115–122, 1999.¶

Bouillon, A., Bernard, M., Gigord, P., Orsoni, A., Rudowski, V. and Baudoin, A.: SPOT 5 HRS geometric performances: Using block adjustment as a key issue to improve quality of DEM generation, ISPRS J. Photogramm. Remote Sens., 60(3), 134–146, doi:10.1016/j.isprsjprs.2006.03.002, 2006.¶

Christianson, K., Bushuk, M., Dutrieux, P., Parizek, B. R., Joughin, I. R., Alley, R. B., Shean, D. E., Abrahamsen, E. P., Anandakrishnan, S., Heywood, K. J., Kim, T.-W., Lee, S. H., Nicholls, K., Stanton, T., Truffer, M., Webber, B. G. M., Jenkins, A., Jacobs, S., Bindschadler, R. and Holland, D. M.: Sensitivity of Pine Island Glacier to observed ocean forcing: PIG response to ocean forcing, Geophys. Res. Lett., 43(20), 10,817–10,825, doi:10.1002/2016GL070500, 2016.¶

Church, J. A., Cazenave, A., Gregory, J. M., Jevrejeva, S., Levermann, A., Merrifield, M. A., Milne, G. A., Nerem, R. S., Nunn, P. D., Payne, A. J., Pfeffer, W. T., Stammer, D. and Unnikrishnan, A. S.: Sea Level Change. [online] Available from: [http://www.ipcc.ch/pdf/assessment-](http://www.ipcc.ch/pdf/assessment-...) ... [1]

1325 **Tables**

| | |
|--|---------------------|
| Convergence angle | 10-60° |
| Time between images | <2 days |
| Minimum intersection area | 100 km ² |
| Minimum relative image area for intersection | 30% |

Table 1: Cross-track stereo pair criteria.

| | Along-track Stereo | | Cross-track stereo | | Combined | |
|--|--------------------|-------|--------------------|------|----------|-------|
| Count | 343 | | 25 | | 368 | |
| Mean offset before/after co-registration (m) | -3.06 | -0.01 | -4.03 | 0.02 | -3.12 | -0.01 |
| Mean RMSE before/after (m) | 3.29 | 0.44 | 5.24 | 0.73 | 3.42 | 0.46 |
| Mean NMAD before/after (m) | 0.36 | 0.36 | 0.63 | 0.63 | 0.38 | 0.38 |

Table 2: Statistics for elevation difference between WorldView/GeoEye DEMs and altimetry control points, before and after DEM co-registration.

| | |
|-----------------------------|-----------|
| Minimum number of DEMs | 4 |
| Minimum total dt | 1.5 years |
| Minimum elevation (EGM2008) | 10 m |
| Maximum absolute dh/dt | 2.0 m/yr |
| Maximum detrended std | 3.0 m |

Table 3: Criteria to identify dynamic control surfaces for least-squares DEM correction. See Figure 5 for resulting map of dynamic control surfaces.

| | Mean (m) | | Median (m) | |
|--|----------|------------|------------|------------|
| | Std. | Detr. Std. | Std. | Detr. Std. |
| Original | 2.45 | 2.11 | 2.49 | 2.08 |
| Co-registered | 1.29 | 0.78 | 0.94 | 0.56 |
| Co-registered and LS "tilt" correction | 1.14 | 0.41 | 0.73 | 0.22 |

Table 4: Results of least-squares DEM correction. Statistics computed for 2010-2015 WorldView/GeoEye DEMs and ATM/LVIS altimetry data over dynamic control surfaces (n=4-44 at each pixel, sample of ~6.1x10⁵ pixels, covering ~4x10⁴ km²). All metrics show decreased spread after correction, with median values less prone to outliers.

Deleted: Figure 4

1330

Figures

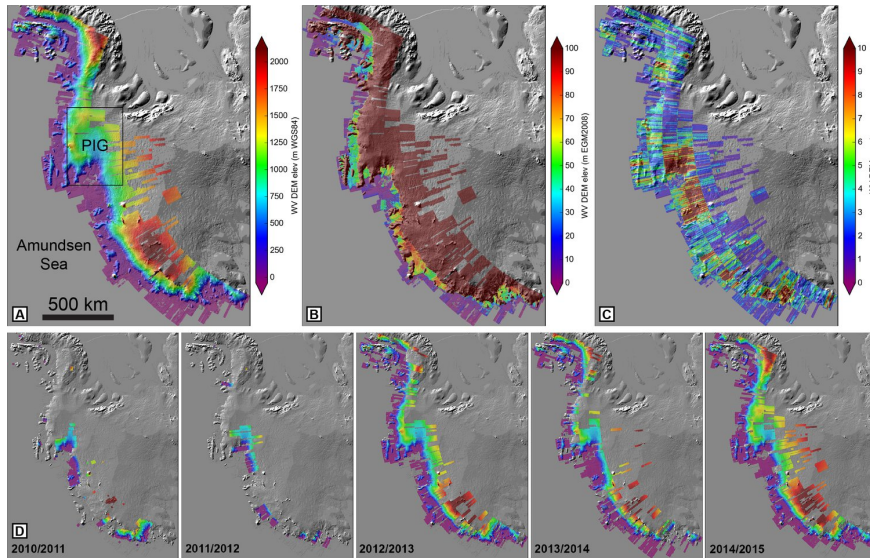


Figure 1: Cumulative and annual DEM composites for West Antarctica. A) Weighted-average composite of ~3000 WorldView/GeoEye stereo DEMs from 2010-2015, overlaid on Bedmap2 shaded relief map. Total cumulative 2-m DEM coverage is 4.1 million km². Black box shows location of Figure 2. B) DEM composite with elevation values relative to EGM2008 geoid (approximates mean sea level) and color stretch to show surface elevation of floating ice shelves. C) Total count of DEMs for the 2010-2015 time period and D) Annual DEM mosaics with same color scale as in panel A. Note increased annual coverage over time, with good coverage of PIG ice shelf in all years. Projection is Antarctic polar stereographic (EPSG:3031).

Deleted: mosaics

Deleted: Cumulative mosaic

Moved (insertion) [1]

Deleted: outline

Deleted: Figure 2

Deleted: mosaic

Deleted: adjusted

Deleted: and stretched

Deleted: over

Deleted: . Note dense coverage over PIG.

Moved up [1]: Total cumulative 2-m DEM coverage is 4.1 million km².

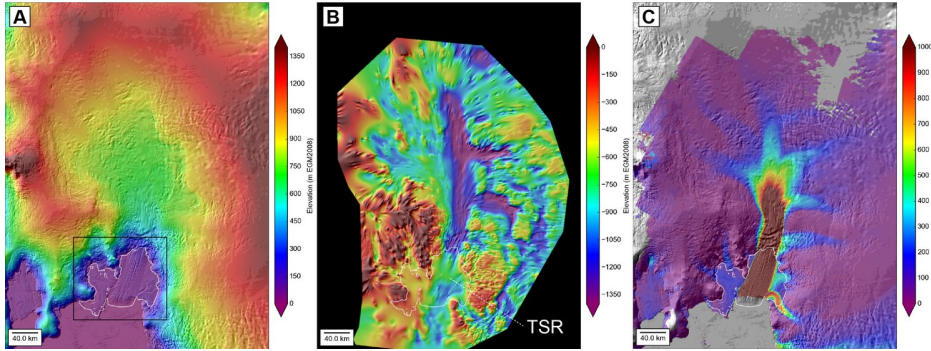


Figure 2: Context for the PIG catchment: A) High-resolution WorldView/GeoEye DEM mosaic over Bedmap2 DEM. White outline shows PIG ice shelf and ~2011 grounding line. Black box shows location of Figure 3. B) Combined bed topography and bathymetry from anisotropic interpolation of radar-derived ice thickness and other sources (see Section 2.6). Note bedrock channels beneath main trunk and tributaries. Dotted white line shows location of transverse seabed ridge (TSR) in PIG ice shelf cavity (see Figure S1 for detailed bed intercomparison). C) Median 2006-2016 surface velocity magnitude with color ramp saturated at 1 km/yr to show detail over tributaries (see Figure 1 of Shean et al. (2017) for color ramp saturated at 4 km/yr).

- Deleted: Surface elevation,
- Deleted: outline
- Deleted: of PIG ice shelf in
- Deleted: panel D
- Deleted:
- Deleted: B
- Deleted: deep
- Deleted: scale

360

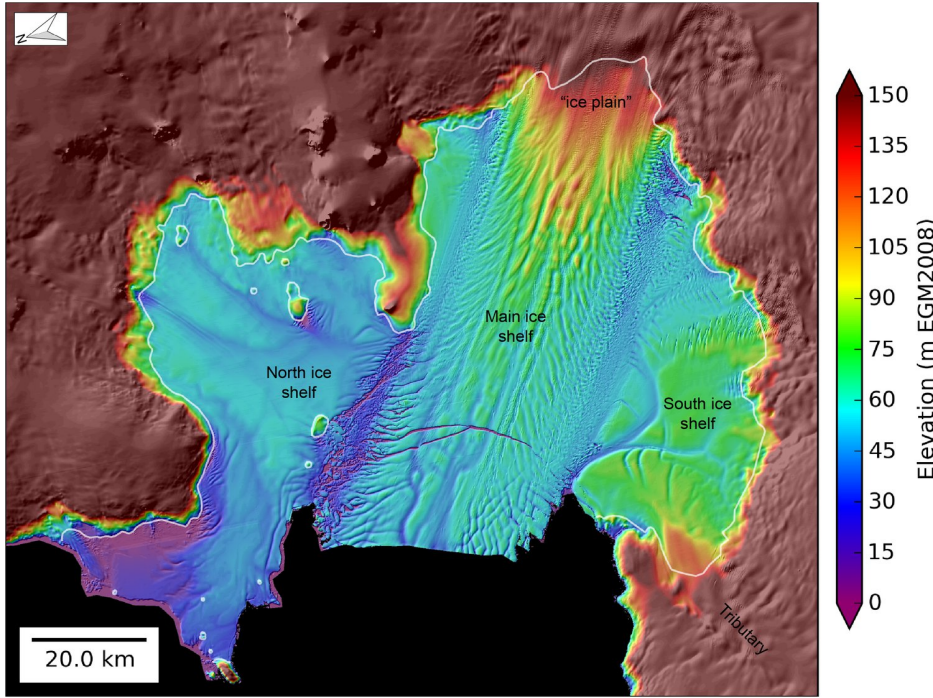
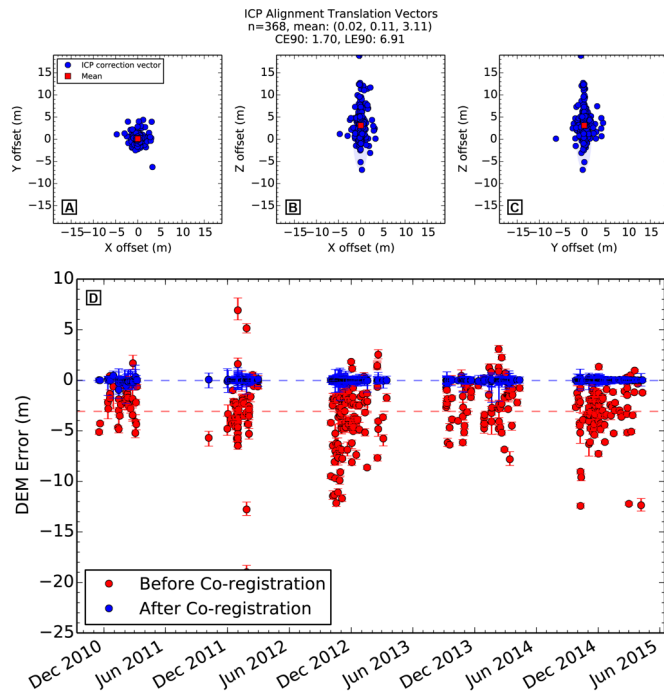


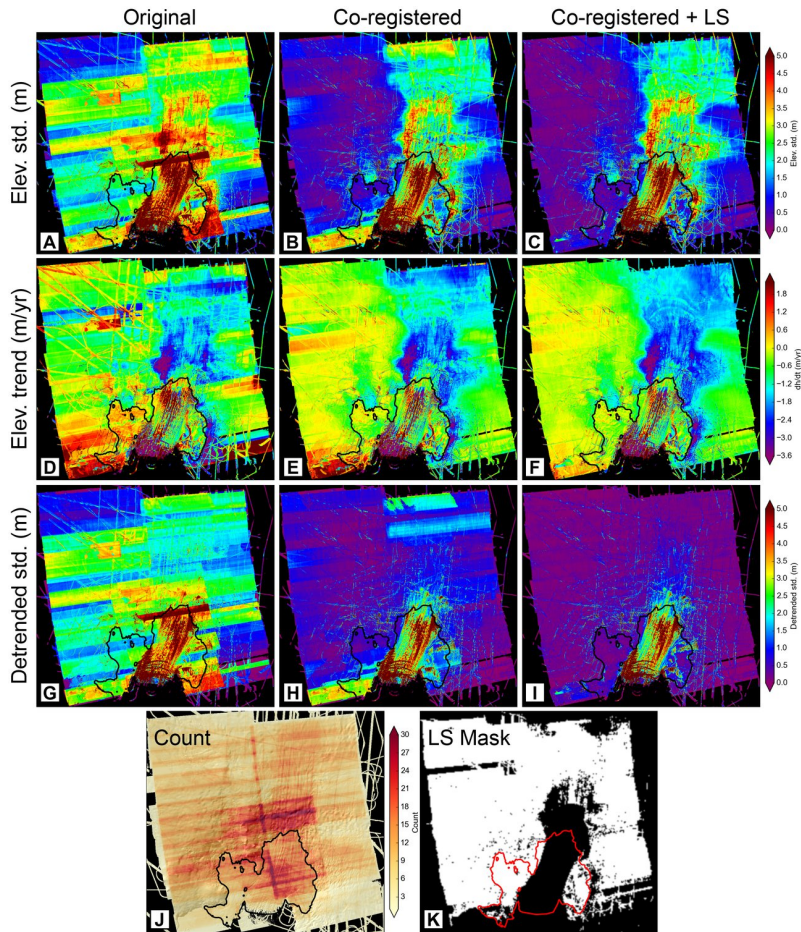
Figure 3: October–December 2012 WorldView/GeoEye DEM mosaic of the PIG ice shelf. Labels show regions discussed in text: North ice shelf, South ice shelf, Main ice shelf, "ice plain", and fast-flowing South ice shelf tributary. White outline shows ~2011 grounding line. Elevation values are corrected surface height (Equation 1) above the EGM2008 geoid.

- Deleted: D)
- Deleted: over
- Deleted: n
- Deleted: (N)
- Deleted: s
- Deleted: (S)
- Deleted: m
- Deleted: (M)
- Deleted: (IP)
- Deleted: (Tributary)



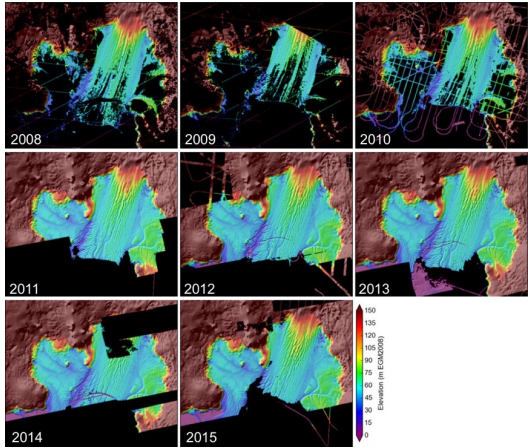
390 **Figure 4:** Co-registration results for 368 WorldView/GeoEye DEMs over PIG catchment (see Shean et al. (2016) for additional
395 details). A-C) Iterative Closest Point (ICP) translation vector components required to co-register each DEM with filtered altimetry
data. D) Median DEM error (DEM - altimetry) with error bars showing 16-84% spread for each DEM, before (red) and after (blue)
co-registration. Horizontal dashed lines show mean error values. The 2011/2012 cross-track stereo DEMs display larger errors
before co-registration. After co-registration, bias is removed and residual error spread for individual DEMs is typically <0.5–1 m,
as summarized in Table 2.

- Deleted: 3
- Deleted: PIG WorldView/GeoEye DEM c
- Deleted: GCP
- Deleted: (see Shean et al. (2016) for details)
- Deleted: Table 2



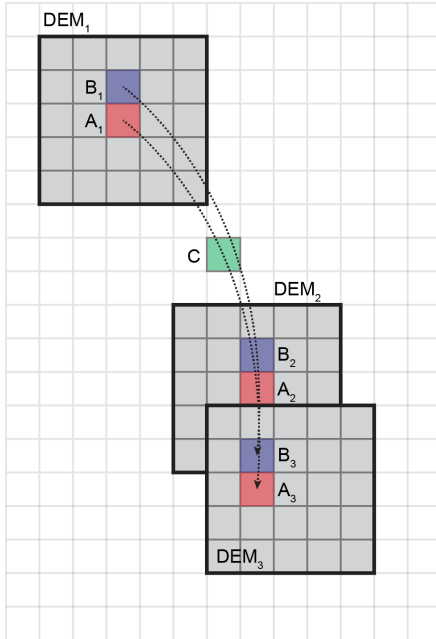
405 Figure 5: Statistics for 2010-2015 WorldView/GeoEye DEMs and available 2009-2015 ATM/LVIS altimetry data over the PIG study
 410 area. Top row (A-C) shows per-pixel elevation standard deviation, second row (D-F) shows per-pixel linear elevation trend, and
 third row (G-I) shows per-pixel standard deviation of residuals from linear regression. Left column (A,D,G) shows values for original
 DEM products before correction, center column (B,E,H) after ICP co-registration to filtered altimetry data, and right column (C,F,I)
 after least-squares optimization to correct residual DEM "tilt". Note overall improvement of final correction (right column). Bottom
 row shows per-pixel DEM count (J) and dynamic control surfaces (white) used during least-squares correction (K), as defined by
 criteria in Table 3.

- Deleted: 4
- Deleted: maps of
- Deleted: at every pixel
- Deleted: "Original"
- Deleted: "Co-registered"
- Deleted: "Co-registered + LS"
- Deleted: Table 3



420 | Figure 6: Annual DEM composites using all available elevation data. Primary DEM sources are SPIRIT (top row), and WorldView/GeoEye (middle and bottom rows).

Deleted: 5

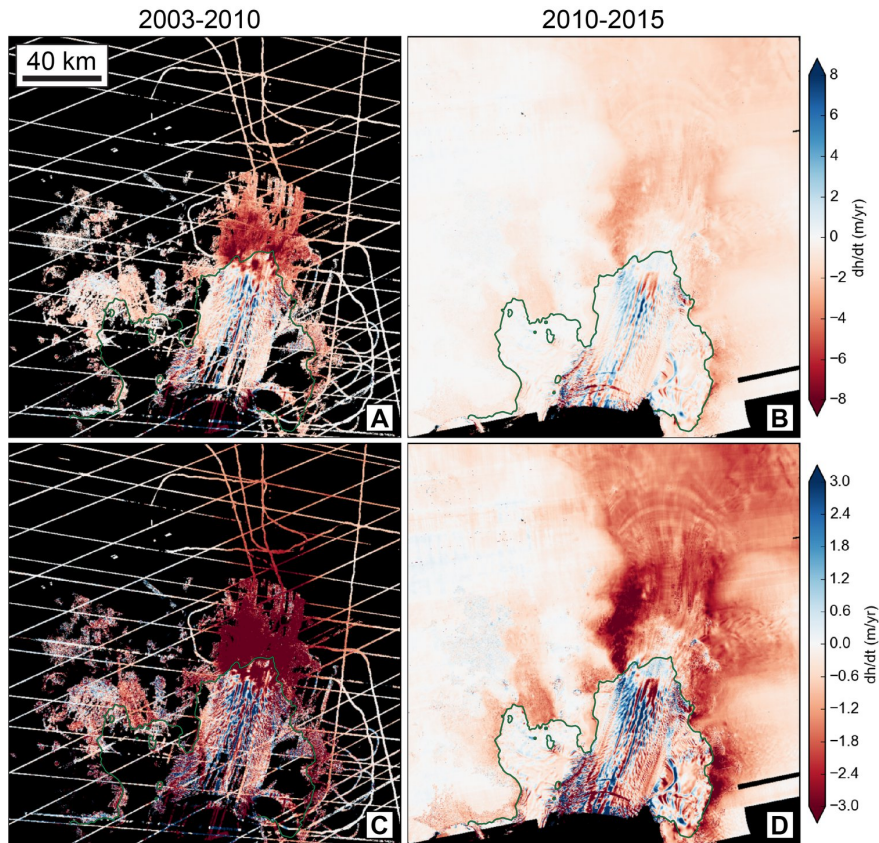


425 Figure 7: Illustration of Lagrangian Dh/Dt calculation and basal melt rate distribution on a Eulerian grid (light gray). Three DEMs
 (medium gray) acquired at times t_1 , t_2 , and t_3 are resampled on this grid, with the same "features" A and B indicated as colored
 pixels. The position history for "particle" A is estimated using the velocity products described in Section 2.5, with paths indicated
 by dotted lines. Lagrangian Dh/Dt for A is calculated as $(h_{A2}-h_{A1})/(t_2-t_1)$. At each timestep along the path from A_1 to A_2 (A_{12}), we
 430 estimate h (from observed Dh/Dt), velocity divergence (from observed velocity time series), and the local flux divergence. Using
 Equations 10 and 12, the cumulative basal melt rate along the A_{12} path is estimated. This procedure is repeated for "particle" B and
 all other "particles" in DEM₁ that intersect DEM₂. For the "along-flow distribution" approach, the cumulative basal melt rate for
 path A_{12} is assigned to each Eulerian grid cell along path A_{12} , including grid cell C. This assignment is repeated for path B_{12} and all
 other paths for DEM₁-DEM₂ particles, so that many basal melt rate values will be assigned to grid cell C. The median basal melt
 435 rate is calculated from all paths intersecting C. This median value at C (and all other grid cells with nonzero path count) are used
 to populate the along-flow distribution basal melt rate map for DEM₁-DEM₂. This process is repeated for DEM₁-DEM₃ and all other
 valid downstream DEM₁-DEM_j combinations for the specified ~2-year time period. The same process is then repeated for all initial
 DEM_i, and full ice shelf composites are generated as described in Section 3.6.1. For the "initial-pixel" approach, the cumulative
 basal melt rate for path A_{12} is assigned to cell A_1 . This process is repeated for the basal melt rate along path A_{13} and all other valid
 440 downstream DEM_j to estimate "initial-pixel" stack median basal melt rate for A_1 , and all other pixels in DEM₁. This "initial-pixel"
 stack median process is repeated for all valid DEM_i, and these products are combined to create full ice shelf composites as described
 in Section 3.6.2.

Deleted: 6

Deleted: -wide

Deleted: -wide

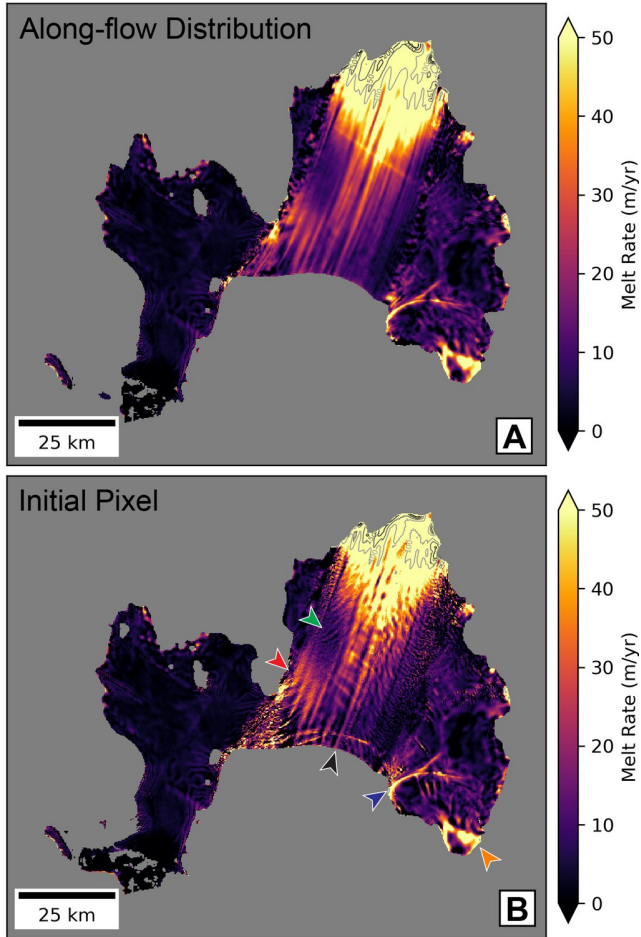


445 | **Figure 8:** Long-term Eulerian dh/dt trends for the PIG ice shelf and lower catchment. A) 2003-2010 dh/dt from ICESat, ATM/LVIS airborne altimetry and SPIRIT DEMs. B) 2010-2015 dh/dt from WorldView/GeoEye DEMs, SPIRIT DEMs and ATM/LVIS airborne altimetry. C+D) Same data as in A+B, but with enhanced contrast stretch to bring out details over main trunk.

Deleted: 7

Deleted: PIG shelf

Deleted: ICESat-1



455 **Figure 2:** Comparison of mean 2008-2015 basal melt rate composites using: A) 2-year "along-flow distribution" and B) 2-year "initial-pixel" methods. Color ramp shows 0-50 m/yr stretch for basal melt rates, with additional grayscale contours at 100, 150, 200 and 250 m/yr near the grounding line. The transverse features along the outer ice shelf centerline in B are related to enhanced melt within and near depressions/rifts (Shean et al., 2017). The transverse mid-ice-shelf artifact in A is the result of a seam artifact in one of the JERSAR-X velocity mosaics. Colored arrows show features discussed in the text.

- Deleted: 8
- Deleted: initial-pixel
- Deleted: along-flow distribution
- Deleted: A
- Deleted: B
- Deleted: TSX

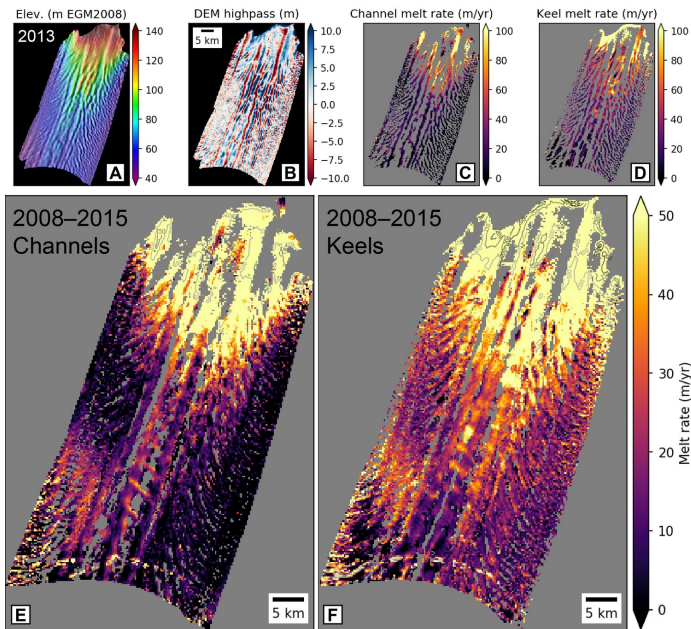
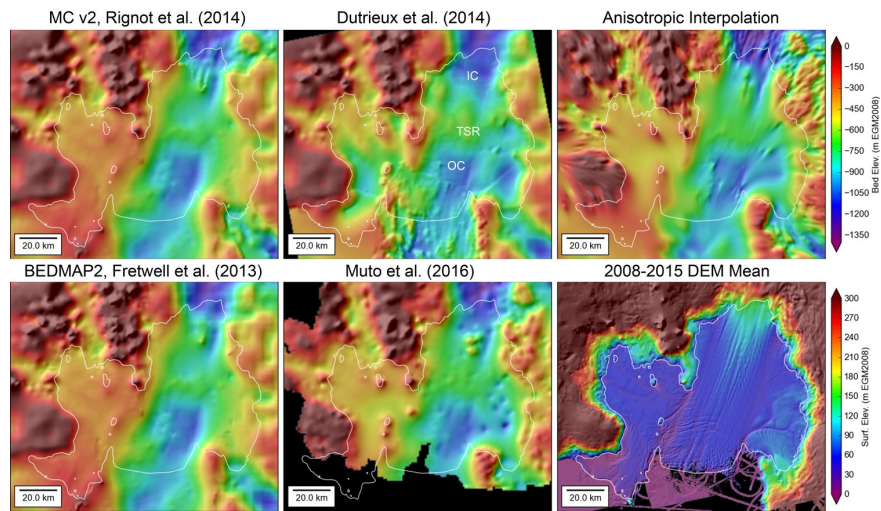


Figure 10: Relationship between km-scale surface ridge/trough (basal keel/channel) features and initial-pixel basal melt rates for main ice shelf. Top row shows example products from one 2-year period (2013–2015): A) 256-m DEM mosaic, B) km-scale surface anomalies after high-pass filter (surface ridges are blue, surface troughs are red), C) basal melt rates for channels (where DEM anomaly is < -1 m), D) basal melt rates for keels (where DEM anomaly is > 1 m). Note relatively high basal melt rates over longitudinal basal channels at distances of ~ 4 – 15 km from the grounding line in C. The bottom row shows channel (E) and keel (F) melt rate composites generated using all available 2-year products during the full 2008 to 2015 period. Color stretch of 0–50 m/yr highlights differences over the outer ice shelf, where higher basal melt rates are observed on keels. See Figure S5 for additional details.

- Deleted: 9
- Deleted: ridge
- Deleted: /trough
- Deleted: features
- Deleted: 2008–2010, second row shows
- Deleted: . First column in these rows shows
- Deleted: second column shows
- Deleted: third column shows
- Deleted: keels (masked where DEM anomaly is > 1 m), fourth column shows...
- Deleted: channels (masked where DEM anomaly is < -1 m).
- Deleted: (low)
- Deleted: (keels) at
- Deleted: 2008–2015
- Deleted: for
- Deleted: basal melt rate
- Deleted: s
- Deleted: over channels and keels
- Deleted: O
- Deleted: (lower)
- Deleted: over
- Deleted: (channels).

Supplementary Figures



5 Figure S1: Comparison of available [combined](#) bathymetry/bed datasets for PIG [ice shelf cavity](#) with mean surface elevation for comparison. See Section 2.6 of main text for details. Top row, center column plot includes labels for "Transverse Seabed Ridge" (TSR), which separates the "Inner Cavity" (IC) and "Outer Cavity" (OC). Note significant differences in inner cavity bathymetry for the different datasets.

ICP Alignment Translation Vectors
 n=5, mean: (18.37, -13.37, -3.64)
 CE90: 40.35, LE90: 8.71

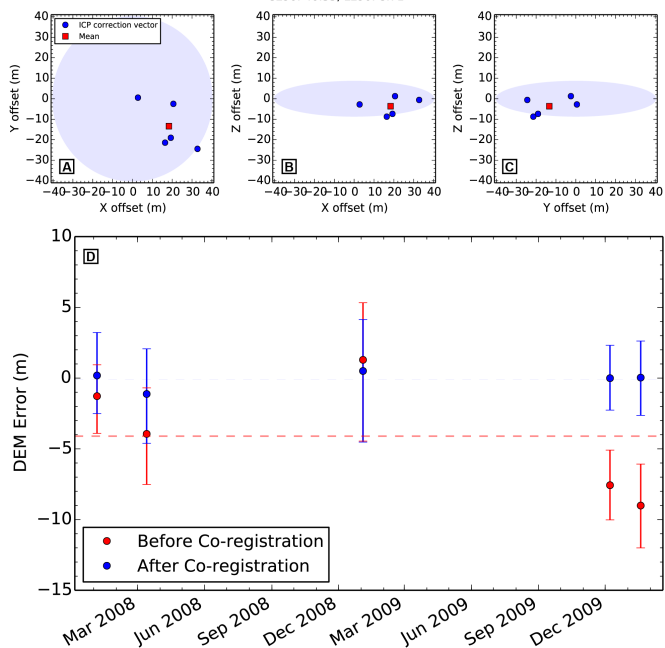


Figure S2: PIG SPIRIT DEM co-registration results. Refer to [Figure 3](#) caption for details.

Deleted: Figure 3

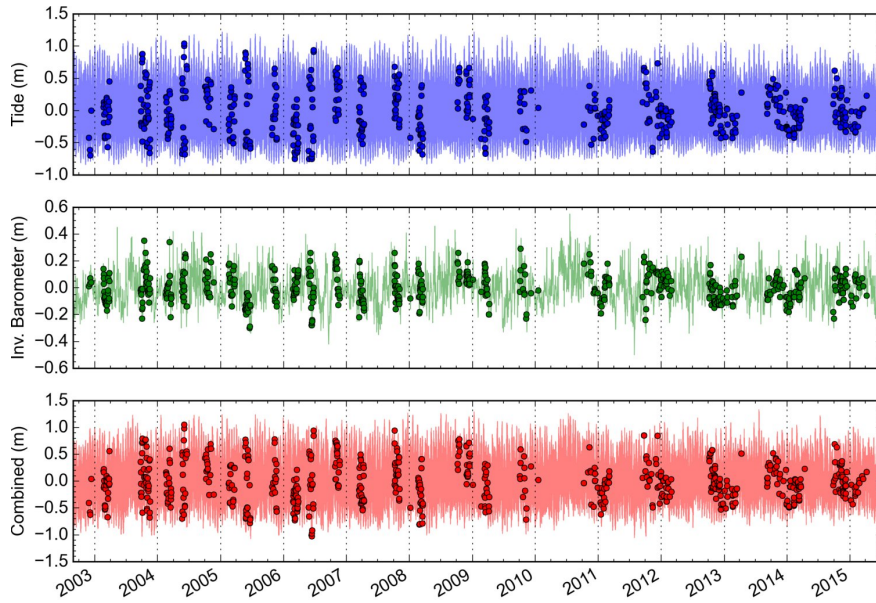


Figure S3: Magnitude of tide and inverse barometer corrections applied to timestamped DEM/altimetry elevation observations (points).

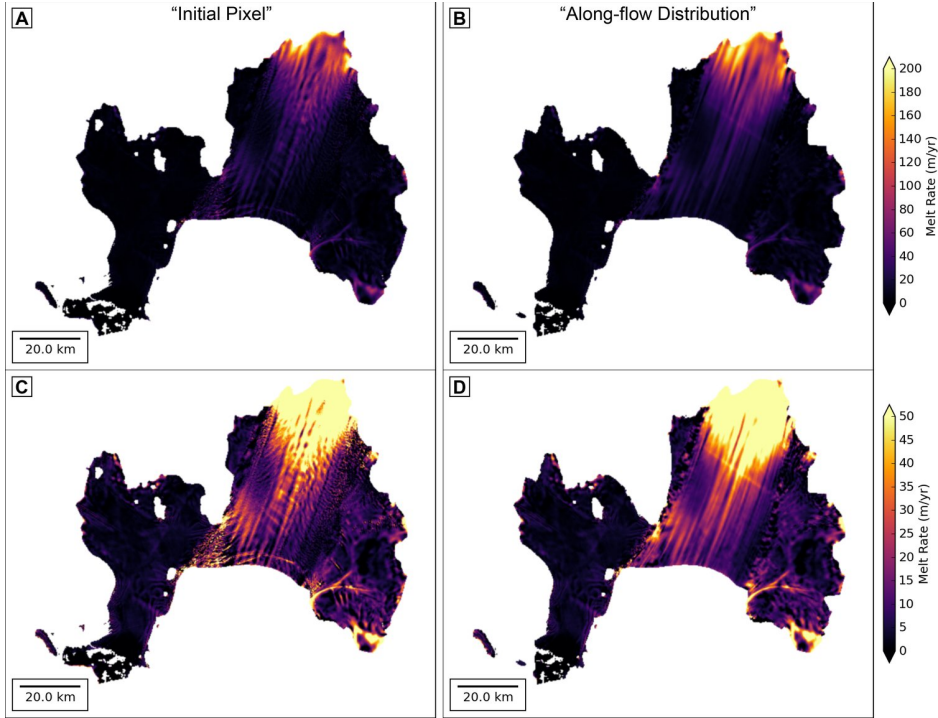


Figure S4: Mean 2008–2015 basal melt rates with different colorbar stretch.

15

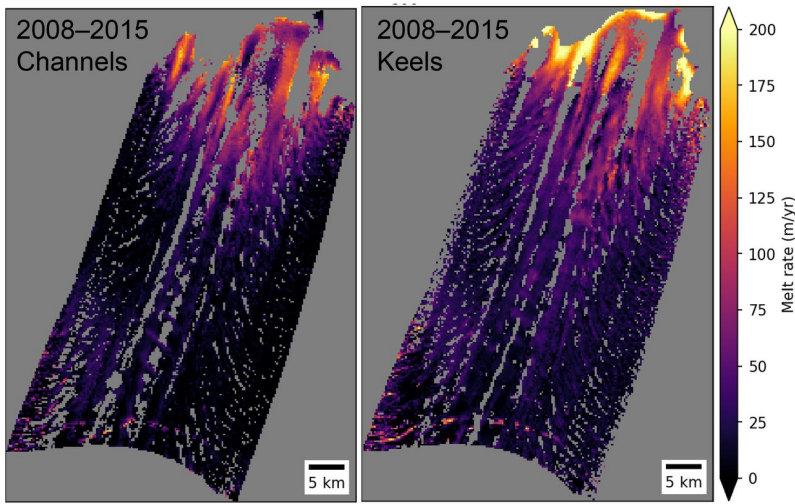
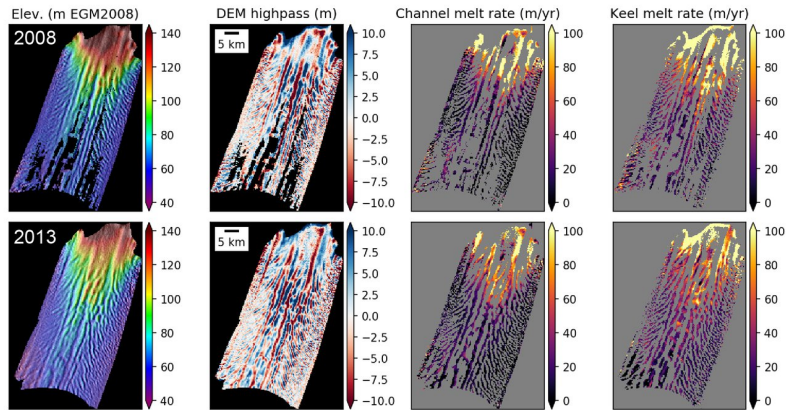


Figure S5: Additional products for channel and keel basal melt rate analysis. See Figure 10 caption in main text. Top row shows initial-pixel melt rate products for 2008–2010, second row show initial-pixel melt rate products for 2013–2015. Bottom row shows 2008–2015 composites for channels and keels, with extended color ramp stretch to bring out details over the inner cavity.

20

- Formatted: Font: Not Bold, English (US)
- Formatted: Font: Not Bold, English (US)
- Formatted: Caption
- Formatted: Font: Not Bold, English (US)
- Formatted: Font: Not Bold, English (US)
- Formatted: Font: Not Bold, English (US)
- Deleted: ¶
- Deleted: ¶
- Formatted: Font: Not Bold, English (US)